Microwave breast tumor detection: simulation and design of experiments with tissue phantoms

Emily Porter

Department of Electrical & Computer Engineering
McGill University
Montréal, Québec, Canada

June 2010

A thesis submitted to McGill University in partial fulfillment of the requirements for the degree of Master's of Electrical Engineering.

Abstract

Recently, microwave imaging has been proposed as a technique for early detection of breast cancer. It is based on the intrinsic contrast in the dielectric properties of healthy and cancerous breast tissues at microwave frequencies. An ultrawideband pulse is transmitted through the breast and a portion of it is scattered when interfaces between two tissues (i.e., fat and tumor) are encountered. The scattered signal is received by antennas surrounding the breast and analyzed to reveal tumor size and location.

This work presents a proposed system for time-domain microwave breast imaging. The components are discussed in detail, with a particular focus on the antennas and radome. Realistic numerical and experimental breast models are constructed for use in validation tests of the proposed system. Simulations and measurements of the antennas behaviour in air, a fat-like medium and radomes of various materials are given. Initial experimental results using complete breast phantoms are presented.

Sommaire

L'imagerie micro-onde a été proposée comme technique pour le dépistage précoce du cancer du sein. Elle est basée sur le contraste intrinsèque entre les propriétés diélectriques des tissus sains et cancéreux du sein pour les fréquences micro-ondes. Une impulsion d'ultra wideband est transmise à travers le sein et une partie du signal est diffusé lorsqu'il rencontre une interface entre deux tissus (par exemple, graisse et tumeur). Le signal dispersé est détecté par des antennes entourant le sein et est analysé afin d'indiquer la taille et l'emplacement de la tumeur.

Ce travail présente une proposition de système pour l'imagerie micro-onde du sein dans le domaine temporel. Les composantes sont décrites en détail, avec une attention particulière sur les antennes et le radôme. Des modèles numériques et expérimentaux réalistes du sein sont construits pour utilisation lors des essais de validation du système proposé. Des simulations et des mesures du comportement d'antennes dans l'air, les milieux reproduisant la graisse et les radômes faits de divers matériaux sont présentées. Des résultats expérimentaux préliminaires employant des fantômes complets du sein sont abordés.

Acknowledgements

I would like to sincerely thank my supervisor, Prof. Milica Popović, for her guidance and encouragement throughout my Master's. I also thank Prof. Coates for meeting with me on a weekly basis to discuss my progress, and Ph.D. student Guangran (Kevin) Zhu for repeated discussions on segmentation and simulation issues. I would also like to acknowledge the support of the Natural Sciences and Engineering Research Council of Canada (NSERC CGS-M).

I must also recognize the hard work of several undergraduate students in assisting me with the phantom mixtures and dielectric measurements: Razvan Oprisor, Jules Fakhoury, Adam Santorelli and Mandy Weigensberg. I thank Mr. Donald Pavlasek (Machine Shop Supervisor, Department of Electrical Engineering, McGill) for his work machining the skin bowls; and M. Jules Gauthier (Superviseur Technique, Polytechnique Montreal) for fabricating the antennas and helping us perform the dielectric measurements on the phantoms. Last but not least, I am grateful to lab manager/post-doc Joshua Schwartz for helping us choose, order and set-up the equipment in our time-domain system.

Table of Contents

Chapter 1 Introduction 1

Chapter 2 Background Literature Review 5

- 2.1 Breast Anatomy and Breast Cancer 5
- 2.2 Review of Measured Breast Parameters 7
- 2.3 Review of Realistic Breast Phantom Construction 12
- 2.4 Review of Microwave Breast Imaging Systems 15

Chapter 3 Proposed System Design 20

Chapter 4 Realistic Numerical Breast Models: Tissue Segmentation from MRI Images 24

Chapter 5 Realistic Experimental Breast Phantoms: Challenges and Solutions 28

- 5.1 Introduction to Tissue Phantoms 28
- 5.2 Design and Fabrication of Skin Bowls 29
- 5.3 Mixture of Tissue Phantoms 31
- 5.4 Phantom Dielectric Property Measurements 33
- 5.5 Construction of Complete Breast Phantom 40

Chapter 6 Antenna Design, Simulations and Measurements 42

- 6.1 Antenna Design and Characteristics 42
- 6.2 Antenna S_{11} Simulations and Measurements in Air 44
- 6.3 Antenna S_{11} Simulations and Measurements in Fat-like Medium 47
- 6.4 Antenna S_{11} Simulations and Measurements in “Suitcase” in Mould 50

Chapter 7 Discussion of Selected Hardware Components 53

- 7.1 Introduction to the Mould 53
- 7.2 Possible Materials for Fabricating Mould 54
- 7.3 Discussion of Mould Shape and Slot Layout 59
- 7.4 Investigation of the Mould with Suitcases 62

Chapter 8 Early Experimental Results 70

Chapter 9 Summary of Works Presented 74

Chapter 10 Conclusion and Future Work 75

Bibliography 76

List of Figures

Figure 2.1. Anatomy of the breast [14]. **6**

Figure 2.2. Median (a) dielectric constant and (b) conductivity measurement results from Lazebnik et al. [15]. The solid line on the graphs represents tissue samples that had 85-100% adipose; the dashed line is 31-84% adipose and dash-dot line is 0-30% adipose. **10**

Figure 2.3. Median (a) dielectric constant and (b) conductivity of malignant tissue measurements from [17]. The solid line represents malignant tissue content of higher than 70%; the dash-dot line at least 50% malignant tissue and the dotted lines at least 30%. **11**

Figure 2.4. Hemi-spherical breast model from Croteau et al. [20]. **14**

Figure 3.1. Schematic of the proposed system. **21**

Figure 3.2. The PicoScope PC Oscilloscope suggested for the experimental set-up. **22**

Figure 3.3. The 8-port Dow-Key Microwave switch. **23**

Figure 3.4. The low-noise amplifier (LNA). **23**

Figure 4.1. An MRI slice with a white square around the area of interest. **25**

Figure 4.2. Segmented breast including skin (left). The manual segmentation of the skin with the area to be removed highlighted in red (centre); and the segmented tissue resulting from the manual segmentation (right). **25**

Figure 4.3. Example of a surface generated in Amira (left) and the SEMCAD model for the same breast (right), where the red portion of the model represents the skin. **26**

Figure 5.1. Photograph of the bowls used to make the skin phantom: closed (left) and open (right). The solidified material that is poured between the bowls mimics the skin. **30**

Figure 5.2. Relative permittivity versus frequency for gland and fat tissue phantoms. Also shown is the median relative permittivity of measurements conducted in [34] on actual fat and glandular tissue. **34**

Figure 5.3. Relative permittivity versus frequency for tumor and skin tissue phantoms. Also shown is the median relative permittivity of measurements on actual skin tissue (from [18], [35]) and actual tumor tissue (from [17]). **34**

Figure 5.4. Conductivity versus frequency for gland and fat tissue phantoms. Also shown is the median conductivity of measurements conducted in [34] on actual fat and glandular tissue. **35**

Figure 5.5. Conductivity versus frequency for tumor and skin tissue phantoms. Also shown is the median conductivity of measurements on actual skin tissue (from [18], [35]) and actual tumor tissue (from [17]). **36**

Figure 5.6. Relative permittivity (top) and conductivity (bottom) versus frequency for the fat phantom showing the standard deviation of measurements. **38**

Figure 5.7. Relative permittivity (top) and conductivity (bottom) versus frequency for the gland phantom showing the standard deviation of measurements. **38**

Figure 5.8. Relative permittivity (top) and conductivity (bottom) versus frequency for the tumor phantom showing the standard deviation of measurements. **39**

Figure 5.9. Relative permittivity (top) and conductivity (bottom) versus frequency for the skin phantom showing the standard deviation of measurements. **39**

Figure 5.10. Photograph of a complete breast phantom including skin, fat, glands and tumor. **41**
Figure 6.1. The TWTLTLA with R_s = 200 Ω/square shown next to a quarter for scale. **43**
Figure 6.2. Plot of the simulated return loss in air versus frequency for four different antenna surface resistivities. **45**
Figure 6.3. Plot of the measured return loss in air versus frequency for four different antenna surface resistivities. **45**
Figure 6.4. Plot of the measured return loss in air versus frequency for eight different 50 Ω/square antennas. **46**
Figure 6.5. Plot of the simulated return loss in a fat-like medium versus frequency for four different antenna surface resistivities. **48**
Figure 6.6. Plot of the measured return loss in a fat-like medium versus frequency for four different antenna surface resistivities. **48**
Figure 6.7. Plot of the measured return loss in a fat-like medium versus frequency for eight different 50 Ω/square antennas. **49**
Figure 6.8. Plot of the simulated return loss for antenna in suitcase in mould versus frequency for four different antenna surface resistivities. **51**
Figure 6.9. Plot of the measured return loss for antenna in suitcase in mould versus frequency for four different antenna surface resistivities. **52**
Figure 7.1. Plot of the simulated return loss versus frequency for four antennas immersed individually in a medium with relative permittivity of 10.2. **57**
Figure 7.2. Plot of the simulated return loss versus frequency for three antennas immersed in a medium with relative permittivity of 4.4 (Lexan). **57**
Figure 7.3. Plot of the simulated return loss versus frequency for three antennas immersed in a medium with relative permittivity of 6.9 (Mycalex). **58**
Figure 7.4. Plot of the simulated return loss versus frequency for four antennas immersed in a medium with relative permittivity of 9.6 (Alumina). **58**
Figure 7.5. Comparison of the simulated return loss versus frequency for a 50 Ω/square antenna immersed in an ideal medium and Alumina. **59**
Figure 7.6. Initial mould design. **60**
Figure 7.7. Updated drawing of the mould. **60**
Figure 7.8. The mould with suitcases in the larger slots. The blue cut-away area from the slots is the size of the suitcases, while the red area is the size of the antenna within. **62**
Figure 7.9. Plot of simulated S_{11} versus frequency for three antennas with a mould made from Lexan and suitcases from HiK. **64**
Figure 7.10. Plot of simulated S_{11} versus frequency for three antennas with a mould made from Mycalex and suitcases from HiK. **64**
Figure 7.11. Plot of simulated S_{11} versus frequency for three antennas with a mould made from Alumina and suitcases from HiK. **65**
Figure 7.12. Plot of simulated S_{11} versus frequency for the 50 Ω/square antenna in a mould of ideal material (blue), a mould of Alumina (green) and a mould made from Alumina with HiK suitcases (red). **65**
Figure 7.13. Drawing of the final mould design. **67**
Figure 7.14. Drawing of the final mould design, rotated 90°. **67**
Figure 7.15. Photograph of the mould. **67**

Figure 7.16. Schematic drawing of the bottom half of the suitcase (drawn by Emerson & Cuming): Back view (top drawing), top view (centre) and front view (bottom). The dimensions for each section are given in inches [centimetres]. **69**
Figure 7.17. Photograph of the suitcase components. Top piece of suitcase (left) and bottom piece (right). **69**
Figure 8.1. Plot of the tumor response when the antennas are embedded directly in the fat phantom. **72**
Figure 8.2. Plot of the tumor response when the antennas are embedded in a fat phantom with skin. **72**
Figure 8.3. Plot of the tumor response when the antennas are in the mould, which holds a fat phantom. **73**
Figure 8.4. Plot of the tumor response when the antennas are in the mould, which holds a fat phantom with skin. **73**

List of Tables

Table 5.1. List of ingredients and the amount used for mixing each tissue phantom. **32**
Table 8.1. List of experimental test cases. **71**

Glossary of Terms

DCIS	Ductal carcinoma in situ
EM	Electromagnetic
FCC	Federal Communications Commission
FDTD	Finite-difference time-domain
IDC	Invasive ductal carcinoma
ILC	Invasive lobular carcinoma
LCIS	Lobular carcinoma in situ
LNA	Low-noise amplifier
MRI	Magnetic resonance imaging
SAR	Specific absorption rate
TWTLTLA	Traveling Wave Tapered and Loaded Transmission Line Antenna
UWB	Ultrawideband
VNA	Vector network analyzer

Chapter 1 Introduction

Breast cancer is one of the most commonly diagnosed cancers in Canadian women, second only to non-melanoma skin cancer [1]. It is estimated that last year in Canada alone there were 22,700 women diagnosed with breast cancer, and 5,400 died from it [1]. This corresponds to an expected one out of nine women who will develop breast cancer during their lives, and one out of twenty-eight will die as a result [1]. Despite these huge numbers, there has been great success in improving the survival of women diagnosed with this disease. In [2], it is noted that, due to improved diagnostic techniques and better treatment options, the death rates due to breast cancer in the United States have decreased by roughly 2% per year over the last decade. If the cancer is detected in time, when it is still localized, the 5-year survival rate, as calculated by the American Cancer Society with statistics from 1996-2003, is 98% [3]. If the cancer has spread into nearby tissue at the time it is diagnosed, the 5-year survival rate decreases to 83.5% [3]. When the cancer metastasizes into distant tissues, the survival rate drops to only 26.7% [3]. These figures clearly show the benefit of early detection: the smaller and more localized a malignant tumor is upon detection, the more successful treatment is.

Currently, some of the most common early detection techniques include X-ray mammography, ultrasound and magnetic resonance imaging (MRI). Mammography, denoted as the “gold standard” [4], is usually the first technique used on a patient. If the mammogram shows irregularities, it is then followed up with ultrasound, or a biopsy, to confirm results [2].

A mammogram is an X-ray picture that is taken of a breast under compression [4]. Through many studies, it has been repeatedly confirmed that the use of mammography decreases the fatality rate due to breast cancer [5].

Despite this, there are several disadvantages associated with X-ray mammography. Depending on the study, between 15% and 34% of lesions are missed by mammograms (this denotes the 'false-negative' rate) [2], [4], [6]. Mammograms also have a false-positive problem: they cannot distinguish between malignant and benign tumors [2]. This is why follow-up tests are required. Since X-ray mammography is effectively a map of tissue densities [4], when the breast tissue is very dense, it is difficult to isolate lesions [5]. Further, X-rays are a source of ionizing radiation, so there are health concerns associated with undergoing mammograms too frequently [4].

Ultrasound is commonly used after an irregularity is found in a mammogram to establish whether it is a non-threatening cyst or a malignant tumor [2]. Ultrasound images are made by sound wave reflections off the body [2]. This technique has the advantages of being non-invasive, involves no ionizing radiation, has portable equipment and is relatively cheap. However it cannot always conclusively identify malignancies, therefore, biopsies are occasionally needed as a follow-up procedure.

Like ultrasound, MRIs are used after mammograms to determine whether abnormalities are harmful or not. MRI is high resolution and non-invasive, but it is very expensive. MRI machines are also large and thus not mobile, and scans can be time-consuming and are inaccessible for regular screening.

It is evident that each of the techniques has their own set of downfalls which does not allow for a single one to be used alone. This underscores the need for an improved technique for early detection of breast cancer. Microwave imaging is one such technique that is currently being researched as an alternative method for detecting malignant tissue inside the breast. It is based on the fact that there is an inherent contrast in the dielectric properties of healthy and tumor tissue at microwave frequencies. In microwave imaging, the breast is illuminated with an electromagnetic (EM) wave and when the EM wave hits an interface of two media with different dielectric properties (for example, fat and tumor), a portion of the wave is transmitted, a portion reflected and a portion absorbed by the tissues. This allows the reflected or transmitted signals to be analyzed to recreate a scattering profile of the breast's dielectric properties. Studies to date show that microwave imaging would have the potential to be non-invasive, safe, and painless. It is particularly useful for breast imaging; since breast tissue is mostly low-loss fat, the attenuation of the propagating signal is relatively small. Microwave imaging also has the potential to be both more sensitive and more specific than traditional detection techniques. However, the difficulty in conducting experiments with microwave breast imaging is that the dielectric properties of various breast tissues are not known conclusively [7], nor is it easy to reproduce their physiological layout.

There are two main types of microwave breast imaging that are currently being explored. The first, called microwave radar imaging, involves illuminating the breast with an ultrawideband (UWB) electromagnetic pulse [8]. The second method is called microwave tomography. Unlike microwave radar imaging, tomographic systems use a narrow frequency band of signals.

Although there are strict power limits for medical devices, microwave breast imaging is unlikely to use enough power to cause any concern. The specific absorption rate (SAR), which has units of Watts/kilogram, is a measure of the power that is absorbed into a volume of human tissue [4]. According to the IEEE Standard C95.1-1999, devices that operate in the 100 kHz – 6 GHz frequency band can have a maximum SAR of 1.6 W/kg, if averaged over 1 g of tissue, and still be safe for humans to be in contact with [4]. To underscore the safeness of microwave breast imaging, it is also noted that a microwave imaging system would use power levels that are 10 to 100 times less than those a person is exposed to by talking on a cell phone [4].

In this project, we use an ultrawideband pulse that is transmitted from one antenna and received at one or more other antennas. Using an UWB frequency spectrum promises high spatial resolution, since bandwidth and resolution are inversely proportional [9]. A typical frequency range would be from about 1-12 GHz. Higher frequencies are associated with higher propagation losses, so frequencies above 12 GHz tend to provide less and less information about structures internal to the breast.

Before performing experiments, simulations are needed as an initial test of the system. We use the finite-difference time-domain (FDTD) method to model our system. FDTD was first introduced in 1966 by Yee [10] and has since become very popular in computational electromagnetics for solving problems of high geometrical complexity. The FDTD method gives solutions to the electric and magnetic fields over time and space by calculating them in an alternating "leapfrog" manner [10]. Since it is a time-domain method, it is a good choice for microwave radar imaging as a single simulation can cover a wide frequency range. In this work, all FDTD simulations were performed using SEMCAD-X (Schmid & Partner Engineering AG), a 3-D FDTD solver [11].

In this thesis, we propose an experimental system design to validate microwave radar detection of breast cancer. A review of experimental systems from the literature is presented, followed by our suggested system. Thereafter, we describe the numerical breast models used in our simulation studies. We further show realistic experimental phantoms that mimic the conductivity and relative permittivity of actual breast tissue. A special antenna that was previously designed for microwave breast imaging is described, and we offer simulations and measurements that characterize its properties. The last designed component of the experimental set-up is the 'mould', which acts as a holder for the antennas. This hardware component is discussed in detail, as its shape and material were both considered carefully before manufacturing. Finally, some early experimental results are reported.

Chapter 2 Background Literature Review

2.1 Breast Anatomy and Breast Cancer

A healthy breast consists mainly of fat tissue surrounding glandular structures that include both the lobules, and the ducts that connect the lobules to the nipple. In each breast there are between 15 and 25 lobes, each containing many smaller lobules [12]. Each lobule, in turn, contains several sac-shaped glands. When a woman is nursing the lobules produce milk and the ducts deliver it to the nipple [13]. Figure 2.1 shows a diagram of the breast anatomy, namely, the chest wall, adipose (fat) tissue, nipple, ducts and lobules. Embedded in the fatty breast tissue there are also lymph nodes, small organs that store white blood cells. The lymph nodes in the breast connect to the rest of the body's lymphatic network through a series of vessels [13]. Lymph nodes are important because they not only contribute to the body's immune system, but they also often provide a route for cancerous growths within the breast to spread to other locations in the body [13].

Breast cancer is an unusually fast cell growth within the breast tissue, often in the epithelium of the lobules and ducts [13]. Frequently, cancerous cells clump together in a tumor. If a cancerous tumor is not identified and treated promptly, it can metastasize (spread into surrounding tissue) making the cancer more difficult to treat. Thus cancers are frequently categorized into non-invasive and invasive groups. Non-invasive cancer means that the growth is localized in a small area, i.e., that it has not yet metastasized into nearby tissues. Invasive cancer has metastasized and is therefore more dangerous and harder to treat [13].

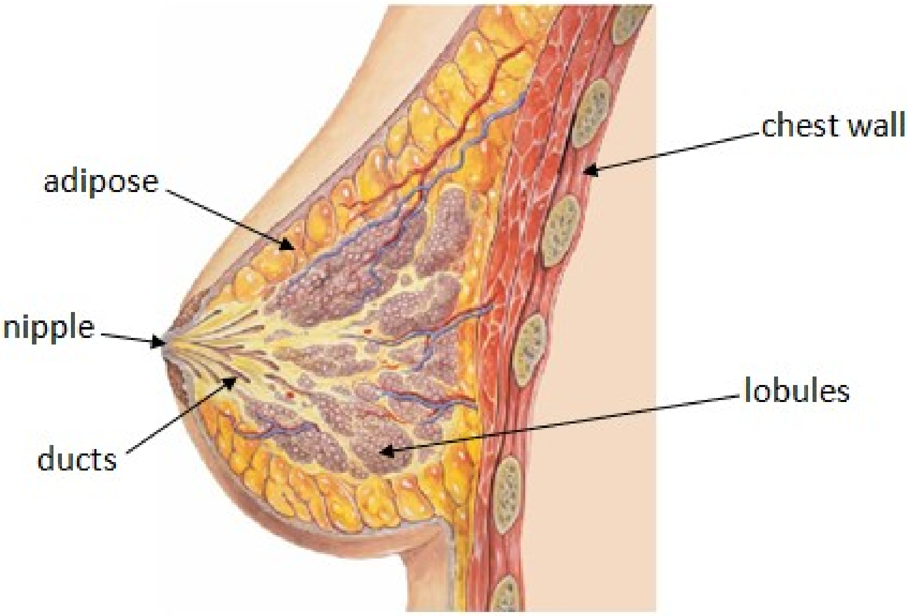

Figure 2.1. Anatomy of the breast [14].

Several types of breast cancer have been identified. The most frequently occurring non-invasive breast cancer is called ductal carcinoma in situ (DCIS) [13]. Carcinoma is the name given to cancers that arise in epithelial tissue. DCIS begins in, and is localized to, the milk ducts. Another type of non-invasive cancer is called lobular carcinoma in situ (LCIS). This disease is caused by cancer cells growing in the lobules. Often it occurs in more than one lobule, but by definition, the cancer has not spread to other areas. DCIS and LCIS by themselves are not grave; however, having either can increase the likelihood of developing other, potentially more dangerous, cancers [13]. A final non-invasive type of breast cancer is called Paget's disease. In this case, cancer cells develop in the ducts just below the nipple and progress to invade the nipple [13].

There are also three main kinds of invasive breast cancers. The most common invasive cancer, like the most common non-invasive cancer, occurs in the ducts. Invasive ductal carcinoma (IDC) makes up roughly three quarters of all diagnoses of invasive breast cancer [13]. On the other hand, invasive lobular carcinoma (ILC) makes up only 10% of all the breast cancers cases that are invasive [13]. Finally, perhaps the most dangerous invasive breast cancer is inflammatory carcinoma. This cancer is characterized by warm, swollen skin caused by cancer cells blocking lymphatic vessels [13]. It grows and spreads very quickly and is easy to misdiagnose, making it one of the most life-threatening breast cancers.

Aside from the various breast cancers discussed above, there are a few rarer conditions that should be mentioned. There are other invasive carcinomas that can occur, namely, tubular, medullary and mucinous cancers [13]. Sarcomas can also appear which, unlike carcinomas, begin in fat, bone or muscle tissue within the breast. These include angiosarcoma and cystosarcoma phylloides [12]. A final type of cancer, called lymphoma, grows immediately in the breast's lymph tissue [12].

It is important to note that non-cancerous cysts develop in the breast as well. These are not harmful but they sometimes have the appearance of malignant tumors in mammograms, a fact which contributes to the difficulty of detecting the presence of cancers. At this point, the breast's physiology has been discussed and the various types of cancers identified, and the focus of this chapter turns to the electrical characterization of breast tissue.

2.2 Review of Measured Breast Parameters

Breast tissue is characterized by two key electrical properties, the relative permittivity, ε_r, and the conductivity, σ. Extensive research has determined that there is a significant contrast between the values of these properties for healthy and malignant breast tissue, particularly in the microwave frequency range. However, identifying the exact relative permittivity or conductivity of a particular tissue type at a certain frequency is difficult, since intrinsic variations in the tissue can be high. This section will review papers that have contributed the most significant measurements of dielectric properties of various breast tissues at microwave frequencies, as well as the measurement techniques and challenges associated with them.

A recent study was performed by Lazebnik et al. in [15], which aimed to characterize the electrical properties of normal (healthy) breast from 0.5 to 20 GHz. This was the first time measurements were taken from such a large number of samples, a total of 354 from 93 patients. The tissue to be measured was taken from newly excised tissue during reduction surgeries. The measurements occurred within five minutes to five hours from the time the tissue was removed from the body. To obtain the measurements, a precision open-ended coaxial probe with a tiny sensing area (depth of 3 mm) was placed on the sample. The probe was connected to either an Agilent 8720ES or Agilent 8722D vector network analyzer (VNA), which recorded the measured values. Following the measurements, the tissue sample's histology was determined by a visual assessment. The samples were categorized into three groups based on the tissue content: group 1 contained samples with 0-30% adipose tissue, group 2 with 31-84% adipose and group 3 with 85% and higher adipose content.

In this work, the measurement results are fitted to a Cole-Cole dispersion model, which is a way to assign an equation to the dispersive tissue properties. While the Cole-Cole model provides an accurate match to measured tissue properties, it is frequently replaced in FDTD simulations by the Debye model, which is much less computationally complex. The corresponding Debye models for these measured tissues are presented in a follow up paper [16].

The Cole-Cole fitted measurement results are reproduced in Figure 2.2. The median of the dielectric constant and the conductivity for each of the three groups is shown. In addition, variance bars representing the 25th and 75th percentile of the measurements for each group are plotted [15]. From these plots, two things can be noted. First, the higher the adipose content of a tissue, the lower its relative permittivity and conductivity are. Secondly, the variation (as seen by the error bars), is quite large, especially for the tissue with a lower percentage of fatty tissue. In fact, the standard deviation of patient-to-patient measurements was 16.17 for dielectric constant and 1.61 S/m for conductivity [15]. It is also found that both the relative permittivity and conductivity decrease slightly in value as the time since excision lengthens [15]. However, overall, the time since excision is determined to be a relatively negligible factor; the same is true with patient age and tissue temperature at the time of measurement [15].

In another study, Lazebnik et al. perform dielectric measurements on breast tissues taken from cancer surgeries [17]. The measurements were conducted in the same manner as in [15], with the exception that for this set of samples the measurements were taken within four hours of the tissue being excised. The cancer surgeries included mastectomies, lumpectomies and biopsies. Thus 85 healthy, 60 malignant and 10 benign samples were collected, for a total of 155 samples from 119 patients. The resulting median dielectric constant and conductivity from the Cole-Cole fitted data for three different percentages of malignant tissue are shown in Figure 2.3 [17]. Samples containing at least 30%, 50% and 70% cancerous tissue were measured, and it is noted that for all three the measurement results are similar. The plot also shows the 25th and 75th percentiles for each of the three concentrations of malignant tissue. It is found that the variations in tissue properties for malignant tissue is relatively small, especially compared to the large variations in the properties of healthy tissue seen in [15].

The study concludes that the contrast in dielectric properties between malignant and mostly adipose tissue can be as high as 10:1 [17]. However, the contrast for malignant and glandular tissues is only around 10% [17]. The variability in dielectric properties due to other factors, such as patient age, sample temperature, and time from excision to measurements were all found to be negligible. The variations from patient to patient and from sample to sample or breast to breast within patient were also determined to be statistically irrelevant.

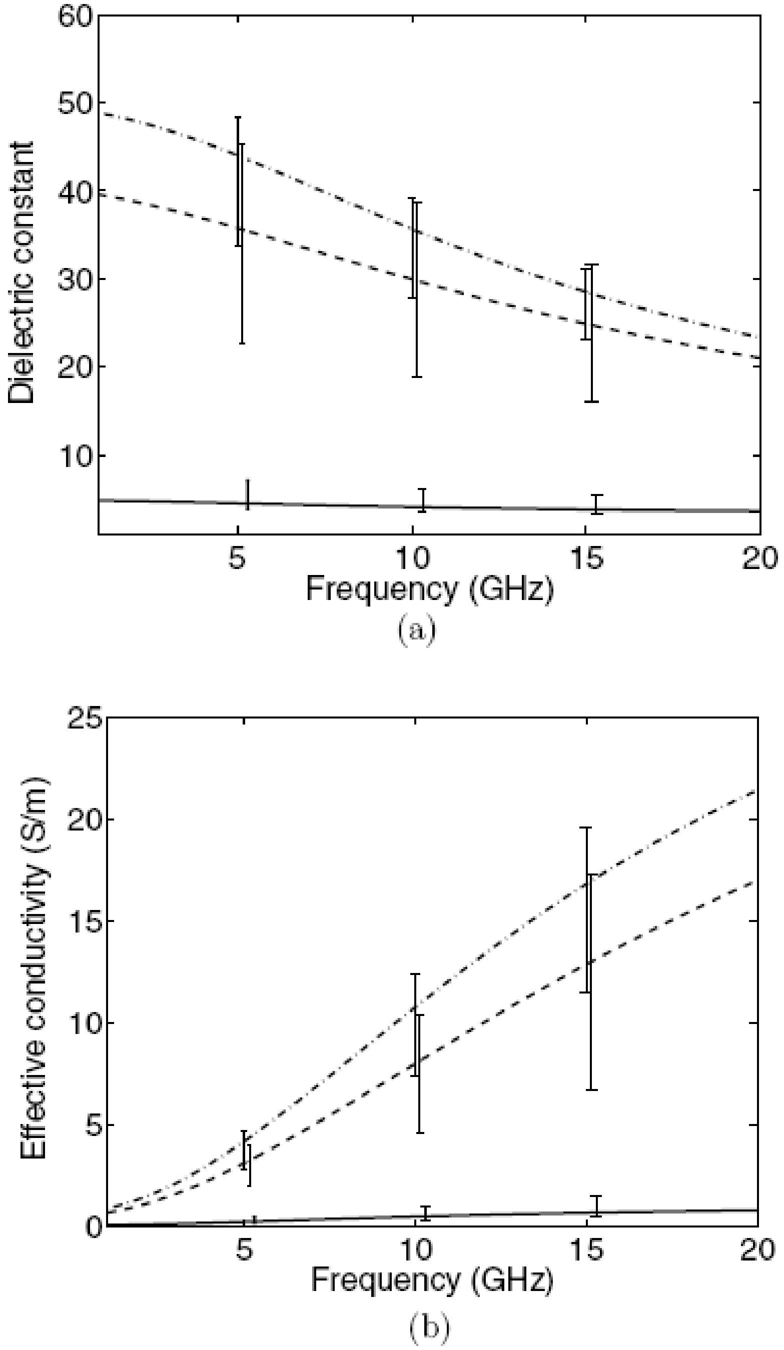

Figure 2.2. Median (a) dielectric constant and (b) conductivity measurement results from Lazebnik et al. [15]. The solid line on the graphs represents tissue samples that had 85-100% adipose; the dashed line is 31-84% adipose and dash-dot line is 0-30% adipose.

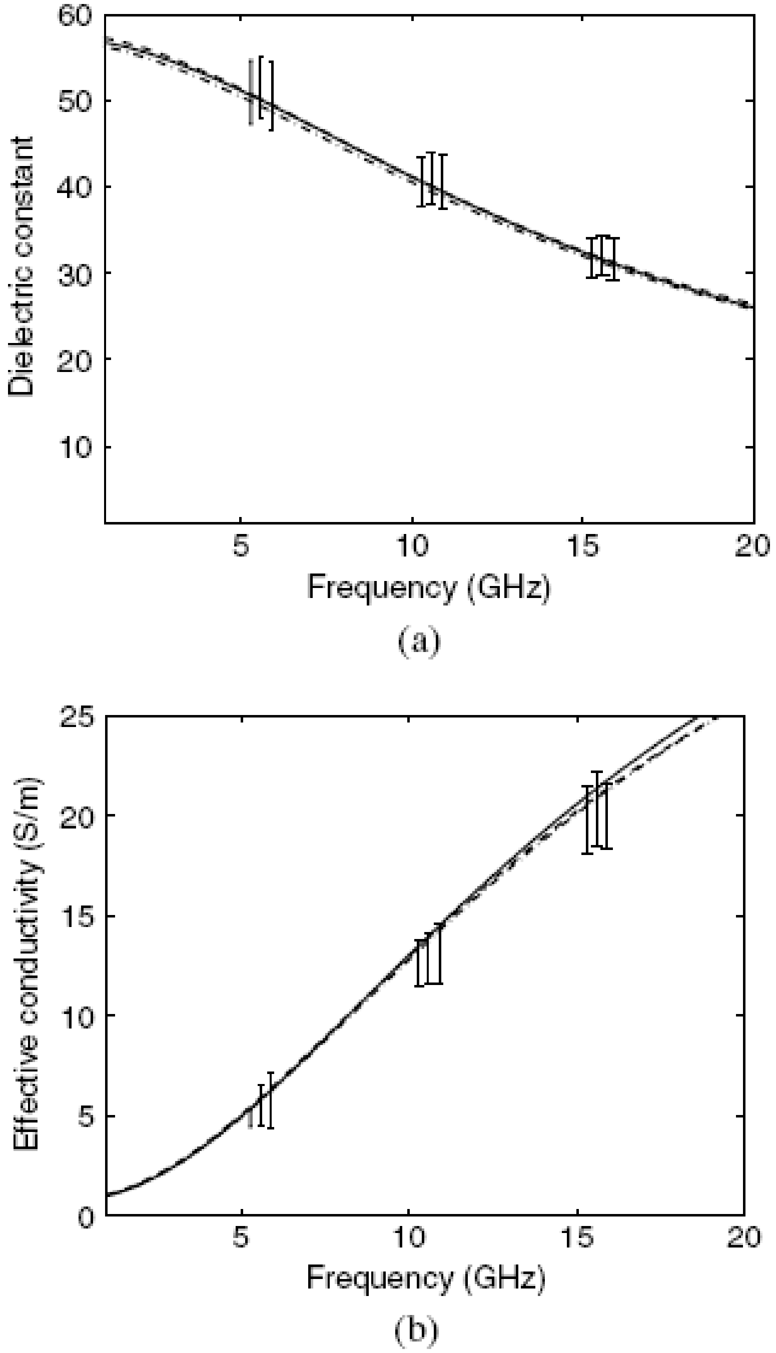

Figure 2.3. Median (a) dielectric constant and (b) conductivity of malignant tissue measurements from [17]. The solid line represents malignant tissue content of higher than 70%; the dash-dot line at least 50% malignant tissue and the dotted lines at least 30%.

These two studies have provided a range within which lies the dielectric constant and conductivity of both healthy and malignant tissues over a wide frequency band. They represent the set of measurements to date with the largest sample sizes, and therefore likely provide the most statistically accurate results. Yet, all of the measurements were made on excised tissue, and in [7] it was shown that the relative permittivity and conductivity both decrease in excised tissue as compared to in vivo measurements. Thus while [15] and [17] have presented a great step forward in terms of knowing the dielectric properties of various breast tissues, it is clear that there is still work to be done towards the ultimate goal of accurately obtaining these properties, for a range of patients and in vivo.

2.3 Review of Realistic Breast Phantom Construction

In this section, papers reporting methods to construct realistic breast models are discussed. We define a realistic model to be one that is accurate in terms of having appropriate tissues incorporated into it, is physically shaped to match actual breast physiology, and has tissue properties that fit with those of measurements performed on real tissue samples. An entirely realistic breast model is desired for microwave imaging validation tests, since early tests cannot be performed on human subjects.

The first paper that addresses construction of realistic tissue phantoms over the UWB microwave spectrum is [18]. In this study, various oil-in-gelatin mixtures are made which are intended to mimic several types of human tissues in terms of their dispersive dielectric properties. Mixtures are made at 10% increments in oil volume, and then their relative permittivity and conductivity are measured from 500 MHz up to 20 GHz. Measurements are done using a vector network analyzer and a hermetic stainless steel borosilicate-glass coaxial probe. For each measurement the probe is placed flat on the phantom surface at room temperature. Three measurements from each phantom are taken and averaged. It is found that by varying the percent volume of oil in the mixture, the dielectric properties of the phantom can be made close to any tissue type. For instance, by comparing with the Cole-Cole models of actual tissue measurements given in [19], it is shown that an 80% oil phantom closely mimics the desired properties for fat, and 25% oil mimics those of skin. It is also noted that a 10% oil mixture approximates the electrical behaviour of malignant tissue. The recipe and instructions for mixing the phantoms are reported in [18].

The results of this study are important for several reasons. A method for constructing tissue phantoms that have realistic relative permittivity and conductivity over a wide frequency range has been given. However what is unique to this paper is that the phantoms are made from widely available materials that are cheap, and the phantoms are easily constructed. The phantoms also have long-term stability, and can be left in contact with each other without changing of dielectric properties thus allowing for heterogeneous phantoms. These results enable the fabrication of breast phantoms that are realistic in terms of dielectric properties as well as geometry.

A second paper, [20], adapts the phantom mixtures presented in [18] and suggests a method for construction of a homogeneous breast model that is dielectrically and physiologically realistic. Phantoms for tumor, skin, gland and fat are mixed with oil concentrations of 10%, 20%, 35% and 80%, respectively. The tissue phantom properties are measured using a dielectric probe attached to a VNA over the frequency range of 50 MHz to 13.51 GHz. For each phantom, two measurements are taken and averaged. It is mentioned that the dielectric properties of the four mixtures match closely to those of the real tissues; however no numerical comparisons are made.

Aside from the four phantom mixtures, [20] also demonstrates a procedure for fabricating a geometrically accurate complete breast model. First, a hemispherical model is made by pouring a liquid skin phantom into a 4” diameter mold and compressing it with a smaller 3.5” diameter bowl. Once the skin solidifies, the smaller bowl is removed and liquid fat is poured into the skin. At this point, a lid with cylindrical rods attached to it is put on top of the bowl such that the fat hardens with holes in it. Then, the tumor or gland mixture, or both, is added via syringe into the holes. A picture of this breast model including skin, fat and glands is shown in Figure 2.4.

Secondly, a more realistically shaped breast model is made using Friendly Plastic, a malleable material that has appropriate electrical properties. The Friendly Plastic is molded to breast shape; so it is no longer hemispherical. Once the mold for the breast is made, the complete model can be constructed the same way as for the hemispherical case. However an added bonus of using Friendly Plastic is that it can also be used to build glandular structures of any shape or size, allowing for potentially more realistic glands. Four realistic models are made - the smallest one is 106 x 90 mm while the largest is 130 x 108 mm. They have a minimum skin thickness of 2.4 mm and a maximum of 2.9 mm.

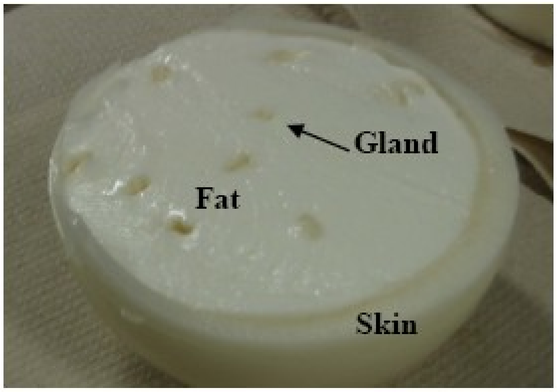

Figure 2.4. Hemi-spherical breast model from Croteau et al. [20].

Overall, this paper reports excellent developments in the construction of realistic breast models. It allows the four tissue phantom types to be incorporated into a single model. It also allows the designer to choose the size and density of gland tissue. However only tumors within gland tissue are described; and the skin thickness is too large in the hemi-spherical phantom (almost 13 mm). Making skin-mimicking material thinner than several millimetres is a challenge, but it would have the benefit of a more realistic breast phantom.

2.4 Review of Microwave Breast Imaging Systems

Through several papers, [21], [22], [23], [24], [25], and [26], I.J. Craddock et al. present the development of their UWB radar imaging system for breast cancer detection. Their design uses 16 stacked patch antennas arranged in a hemispherical 4 by 4 pattern. The radius of the sphere used is 78 mm, and the antennas are located covering roughly the bottom third of such a sphere. The antennas are cavity backed to reduce reflections, and have S_{11} characteristics lower than -3 dB over the 4 to 9 GHz range. In earlier papers, the rows of antennas are slightly offset in order to provide enough space for connectors and cabling, so the array is not symmetric. However, more recently in [23], the antennas have been reduced in size and thus are aligned symmetrically in 4 rows and 4 columns. The antennas are connected to a set of electromechanical switches that turn on or off in succession each of the possible antenna pairs (one transmitting and one receiving). The switches feed into a VNA which does a frequency sweep from 4 to 10 GHz, records the scattering parameter S_{21} (forward voltage gain), and sends these results to the computer for analysis.

For initial experiments, a breast phantom is placed into the hemispherical antenna array filled with a fat-mimicking matching liquid. The phantoms used have a radius of 58 mm, and are located 2 cm above the antennas. Each phantom has a 2-mm thick layer of skin-like material with a relative permittivity of about 30 at 6 GHz. Inside the ‘skin’ is a fat-mimicking phantom that has a relative permittivity of 10 and an attenuation of 0.8 dB/cm at 6 GHz. Embedded in the fat phantom is a spherical tumor phantom, with a relative permittivity of

50, which is either 4 mm or 10 mm in size depending on the phantom. Thus the contrast between fat mimicking phantom (representing healthy tissue) and the tumor mimicking phantom is about 1:5, which is large when compared to the most recent measurements [25]. None of the phantoms tested included gland-like materials.

Measurements are recorded for each antenna pair, with no monostatic measurements. For 16 antennas, this results in $\frac{16(16-1)}{2} = 120$ unique signals, and this relatively large number minimizes the effects of clutter [24]. A scan of all 120 signals takes only about three minutes. In addition, after the first full scan, the antenna array is physically rotated so that undesirable signals (skin reflection and antenna coupling, for instance) are at approximately the same time position for both the original and rotated data. The original and rotated signals can then be subtracted from each other, effectively removing the unwanted portion of the signals.

By processing the two scans of 120 signals each, a 3-D breast image is obtained. It is seen that the system is capable of detecting both the 10 mm and 4 mm tumor phantoms. The main limitation of the studies to date is that the breast phantoms that are used are not very realistic as the contrast between tumor and fat is over-estimated, and there are no glands which tend to make tumor localization more difficult.

Recently, the system has undergone a small clinical trial [26]. In this series of tests, a 31-element hemispherical (radius = 67 mm) antenna array is used. The antennas are cavity backed ultrawideband slot antennas. Initial results are good; however several difficulties with performing measurements in a clinical setting are noted. For instance, patient movement and breathing can negatively affect the quality of the scan. Other challenges include that the breast fit to the array is never perfect and the breast tissue may be more heterogeneous than were the phantoms [26].

A different experimental set-up is given by S. Salvador and her colleagues in [27]. Two types of antennas are explored, a Vivaldi and a dipole antenna, each taking measurements at eight different locations (45° apart). The dipole antenna has smaller dimensions, and thus was the preferred choice. The antenna is connected to a network analyzer which sends the collected data to a computer. As in Craddock's system, Salvador's measurements are all recorded on the network analyzer via a frequency sweep. However here, the frequency range is from 0.1 to 9 GHz (1601 data points) and it is the S_{11} parameter, not S_{12}, which is recorded. For each location at every frequency, the final value determined for S_{11} is given as the average of 16 measurements.

The breast phantoms are made as a 50:50 combination of water and wheat flour with a relative permittivity of just above 70 at 6 GHz; so that their dielectric behaviour approximates closely gland tissue rather than fat tissue. The phantoms are made in conical shapes with a height of 12 cm, maximum diameter of 8.5 cm and minimum diameter of 6 cm. The tumors are made from narrow cylinders filled with water that are placed into the conical breast phantom. The breast and tumor phantoms have a contrast in dielectric properties of about 1.65 to 1 at low frequencies, which is realistic. While several coupling media were tested, alcohol was chosen for both antennas since it gave the best S_{11} values and detection ability. Since it would be undesirable to have alcohol in contact with a patient's skin, a cushion is design which is filled with alcohol and which holds the antenna. The cushion can then be placed against the breast with good contact.

The experimental results show that both 2 cm and 1 cm sized tumors can be detected and properly located. However since the antenna locations are along a single plane, the tumor site is only known in two-dimensions. Also, the breast phantoms used in this study were not very accurate in shape, nor did they include skin. The dielectric permittivity of the breast phantom was much higher than in other studies, for example [23], and may not provide a good approximation to actual breast tissue. Since the best coupling medium depends on the breast properties, it is noted that alcohol may not be a suitable matching liquid for lower permittivity phantoms. One final point of interest is brought up in the paper: the data collected from the frequency range 0.1 to 1 GHz is critical for tumor detection, and the data from 1 to 9 GHz does not add any useful information. However this effect may also be due to the choice of coupling liquid.

A final set-up worthy of discussion is that presented by P. Meaney et al. first in [28] and then more recently in [29]. In the original publication, [28], a 2-D imaging system is presented that is used for monitoring during chemotherapy. An array of 16 monopole antennas is used for this tomographic microwave imaging system. At any given time one antenna is transmitting a signal while all of the others are receiving. The transmitting signal is then alternated through matched switches to all of the 16 antennas. The antennas are located around the breast along a sphere of 7.5 cm radius. Measurements are taken in 100 MHz increments from 300 to 900 MHz at seven different heights of the array. The system was built as a clinical prototype and involved the scanning of five volunteers, with a scan taking 10 to 15 minutes for each breast. The complete scanner has the advantage of being built to fit onto a single cart so that it is relatively portable.

The matching medium used was a 0.9% saline solution, chosen for its wide availability and reasonable cost. The solution has a high relative permittivity in comparison with expected breast tissue values, which may be a disadvantage for imaging some breasts. Despite this, the images obtained from patient scans are determined to be encouraging, reporting a spatial resolution of up to 1 cm and ability to detect formations as small as 0.4 cm in size. This study is definitely promising, however is lacking direct comparison to more accurate results, i.e. MRIs or mammograms, and is not tested with phantoms (where things such as tumor size and location can be definitively known beforehand).

Meaney's more recent paper [29] presents improvements on the original system design. There are still 16 monopole antennas that scan tomographically at 7 different planes. This time, the coupling medium is a mixture of glycerin and water. There are no breast phantoms involved in the experiments; instead scans are done on patients, with corresponding MRIs performed as well. Two-dimensional scans are done and are compared to the MRIs, showing similarities in the tumor size and location. Each of the 2-D images is constructed in less than 3 minutes. Currently, a 3-D scanner is being worked on. It will also have the 16 monopole antennas, and they will be controlled by the computer and moved with motors to different heights. While this paper shows the potential for microwave tomography, no firm numbers are given for either detectable tumor size or localization. Also, neither of the papers explain what other equipment was used in the recording of the signals.

The above discussion has provided a summary of three different possible experimental set-ups for microwave imaging of the breast. It has included description of the antennas, antenna array, equipment and types of phantoms used. Matching mediums between the antennas and the breast surface were also described. The presented systems are lacking in terms of having realistic breast phantoms and underscore the need to have a complete set-up that incorporates accurate models for detection validation.

Chapter 3 Proposed System Design

The motivation for our work is an at-home early-warning system for breast cancer detection. Ideally, it would be a bra-shaped system that a woman could wear for a few minutes every month in the comfort of her own home. Each time a signal is recorded, it would compare it with a previously established ‘healthy’ baseline, and if an irregularity is detected, the system would alert the woman to visit her doctor for further, more detailed examination.

This thesis presents a set-up for initial experiments on microwave radar imaging of the breast in time domain. This system is not miniaturized to be sufficient for the end-stage goal of an at home portable device; it is the first step towards that goal. There are several components in the proposed system, some of which are standard, easily obtainable equipment and others designed and built specifically for this purpose. The planned experimental system and each of its components are discussed through the rest of this chapter.

The idea behind the experiments is to send a brief electromagnetic pulse through a transmitting antenna located near the breast surface. The signal propagates through the impedance-matching medium, into a breast model (phantom), is scattered and picked up by one or several receiving antennas. The antennas may either be opposite each other (the transmission signal is recorded) or beside each other (reflection/scattering). The received signals are then fed into a computer for analysis and processing.

A full schematic drawing of the proposed system is shown in Figure 3.1. The sine wave generator provides the clock for both the impulse generator and the picoscope. During each clock cycle, the impulse generator transmits an impulse to a switch which selects one antenna as the transmitter. The signal is then emitted from that antenna into a matching medium that has dielectric properties similar to those of the antenna’s substrate and the average of the breast tissues. In the schematic, the antennas are held in place by a radome in which the matching medium and breast phantom are positioned. The EM wave propagates through the matching medium into the breast phantom, where it is scattered in different directions. After the portions of the scattered signal leave the phantom, they propagate through the matching medium prior to being detected by the receiving antennas. These received signals are then amplified by low-noise amplifiers, and a switch sends each amplified signal to the picoscope. The picoscope interfaces with the computer, which can then record and store the data.

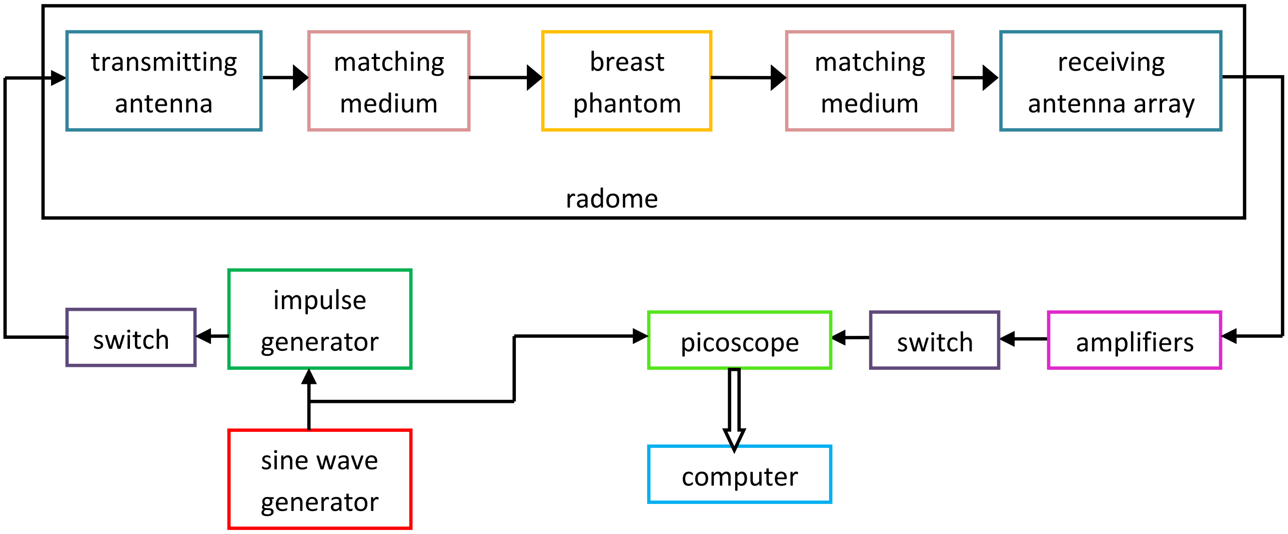

Figure 3.1. Schematic of the proposed system.

The sine wave generator used in our experiments is an Anritsu MG3692B 20 GHz Signal Generator. The output is divided using a 3 dB power splitter, Mini-Circuits ZFSC-2-10G, which operates from 2 to 10 GHz, so that the sine wave can be transmitted to both the PicoScope 9201 PC Oscilloscope (Figure 3.2) and the Picosecond Impulse Generator (model 3600). The maximum input to the picoscope clock (‘prescale’ port) is 2 $V_{p\text{-}p}$ from 1 GHz to 7 GHz, and 1 $V_{p\text{-}p}$ from 7 GHz to 10 GHz. This leads us to place a 12 dB attenuator in the path between the sine wave generator and the picoscope to ensure that the clock signal is at no time higher than the allowable input. At each period of the clock, the impulse generator sends a pulse with amplitude of -7.5 V through a cable to the transmitting antenna.

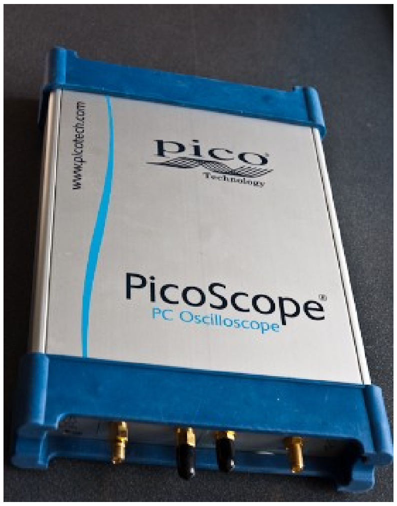

Figure 3.2. The PicoScope PC Oscilloscope suggested for the experimental set-up.

The two switches used are Dow-Key Microwave 581-4908 D/C 0938. Each switch has 8 ports that can be switched between, with a control voltage of 15 V. A photograph of one of the switches is shown in Figure 3.3. The amplifiers, obtained from CCT INC (part number AMX/00510-2524), are low-noise amplifiers (LNAs) (Figure 3.4), necessary since our signal of interest (the tumor response) may be very close to the noise level. The amplifiers are functional from 0.5 to 10 GHz, with a minimum gain of 24 dB. Both the switches and amplifiers have SMA connectors, and thus are easily integrated into the rest of our system. A 15 V DC source is needed to power the amplifiers and switches; we obtain one with a 3 A rating (the eight LNAs draw 120 mA each and the switches 550 mA, so 8(120 mA)+2(550 mA) = 2.06 A of current needed).

The radome, explored in more detail Chapter 7, was designed specifically for this application. It can hold 16 antennas; distributed symmetrically along its spherical geometry. At any particular instance, one of these antennas transmits while the other 15 are receiving signals. The antennas used are described in Chapter 6. Inside the radome, there is an accessible gap for a thin layer of matching medium between the radome wall and the breast phantom. The purpose of the matching medium and its properties are presented in Chapter 5 along with the specifics of the realistic breast model.

Figure 3.3. The 8-port Dow-Key Microwave switch.

Figure 3.4. The low-noise amplifier (LNA).

In this chapter, we presented a time-domain system for microwave radar imaging. Throughout this work, description of the hardware will be given with varying detail, but the signal-processing stage and the related techniques are omitted as they are outside of the scope of this thesis.

Chapter 4 Realistic Numerical Breast Models: Tissue Segmentation from MRI Images

In this chapter, the construction of numerical breast models for finite-difference time-domain (FDTD) simulations is presented. In order to test the feasibility of microwave imaging for breast cancer detection, simulations involving realistic breast models are required. An adequate model should have geometrical and electrical characteristics as close as possible to those of real human breast tissues. Our numerical model addresses both of these aspects; however the focus in this thesis is on the geometrical properties.

MRIs from actual patients with breast cancer are obtained, and act as the basis of the model. In an MRI scan, cross-sectional 2-D images ("slices") are recorded and stacked to obtain a full 3-D image. A typical scan will include both breasts and will have 60 or more slices. Images are grayscale, but the intensity of each pixel can be correlated with the tissue type at that location. In this work, we only use high contrast MRIs obtained from axial scans.

To start, each MRI slice is cropped such that only a single breast's area appears. An example of a slice is shown in Figure 4.1, with the white square enclosing the area to be kept, while the rest of the image is cropped out. Each set of cropped slices is then imported into Amira (Visage Imaging), software that aligns and orders each of the slices and allows for easy segmentation of different tissue types. The breast is first segmented from the background; this is done automatically by Amira. Once the breast shape is defined, the next step is manual segmentation of the skin. Skin does not appear well on MRIs, so the skin thickness is estimated. It has been shown that healthy skin has a thickness between 0.5 mm and 2.5 mm [30]. Since a typical MRI pixel is $0.625 \times 0.625 \times 2\ \text{mm}^3$, a hand-drawn segmentation line between the skin and the interior breast tissue is drawn two to three pixels thick. In this way, the skin thickness varies over the breast with an average near 1.5 mm, but at no point is it thicker than 2.5 mm. This process is illustrated in Figure 4.2, showing a slice with the original breast image as well as the same slice where the skin is highlighted and finally removed. Depending on the breast model, malignant tissue, muscle and chest wall were also segmented.

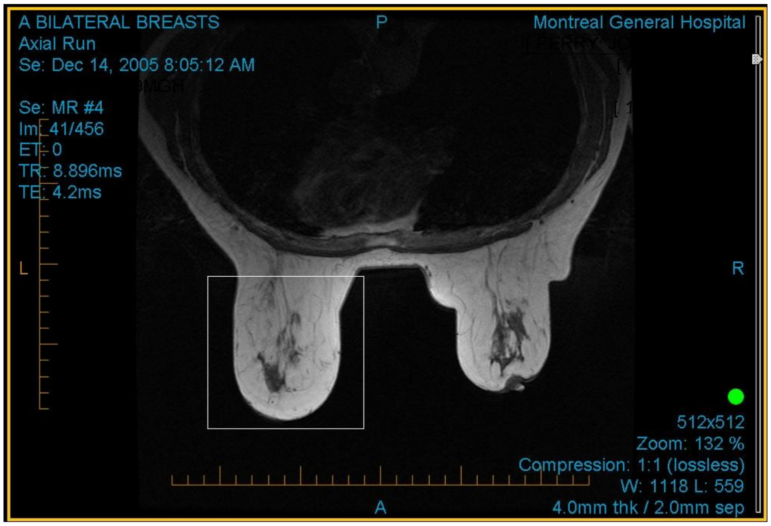

Figure 4.1. An MRI slice with a white square around the area of interest.

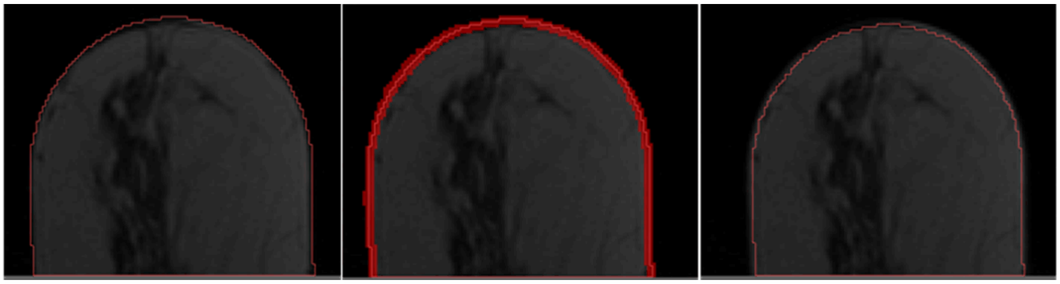

Figure 4.2. Segmented breast including skin (left). The manual segmentation of the skin with the area to be removed highlighted in red (centre); and the segmented tissue resulting from the manual segmentation (right).

Following the segmentation of all tissue types, each defined tissue is converted into a surface. This is done using the “SurfaceGen” command in Amira with unconstrained smoothing, which builds the surface using triangular faces over the tissue segmentations. For the full breast including skin, 7000 triangular faces were used to estimate the surface, and for the tissue without skin only

5000 faces. At this point, the surfaces are imported into SEMCAD, where they can be turned into solids using the “convert polyhedron to body” option. Once in SEMCAD, the full breast and the breast without skin solids can be subtracted to isolate the skin surface. Figure 4.3 shows the breast surface in Amira, as well as the breast volume generated in SEMCAD with the skin outline clearly visible in red. In total, several models were made of each of the healthy breasts and of the breasts containing tumors.

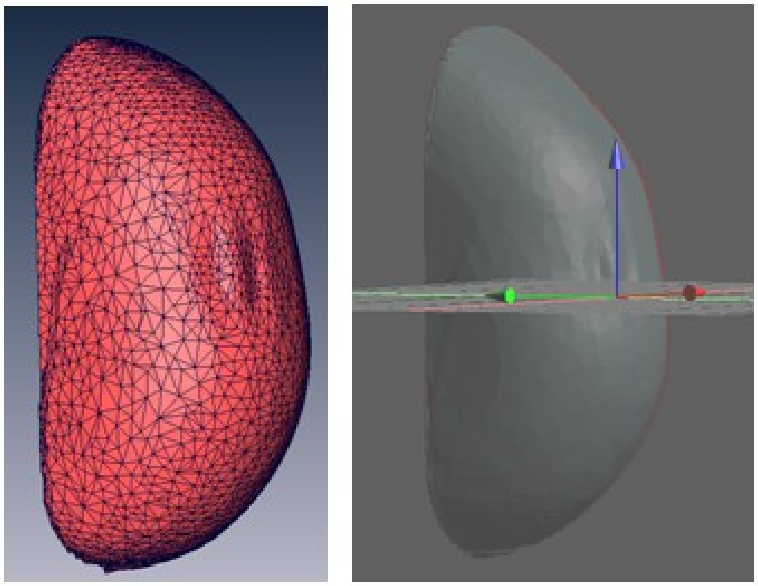

Figure 4.3. Example of a surface generated in Amira (left) and the SEMCAD model for the same breast (right), where the red portion of the model represents the skin.

It is also noted that the breast volume is not entirely smooth, and a “stair-casing” effect can be seen towards the sides of the model. This is due to the discrete nature of MRI slices. Since slices have a finite distance between them, when the breast shape changes quickly, the slices do not reflect that change in a smooth manner. Despite the small stair-casing effect, these models are a much more accurate representation of the human breast than the cylindrical or hemispherical models that have been used in the past.

The biggest challenge encountered in preparing breast models in this fashion is that most of the segmenting must be done manually. This means that for each breast model, one must segment tissues in more than 60 images. It is tedious work, and can be very time consuming. Once the segmenting is complete, however, the surface and solid construction is very quick. To completely build one model from start to finish it can take as much as four or five hours. Since we had only eight models, however, this technique was an acceptable approach.

Up to this point, the focus has been on the physical shape of the numerical breast model. For a truly realistic model, the tissue composition (glands, fat) and the electrical tissue properties (relative permittivity and conductivity) must also be investigated. The composition can be assigned to the solid breast model by looking at the intensity of each MRI pixel, and the properties assigned to each tissue chosen to match those of recent studies. Such work is not within the scope of this thesis; however, details of the process can be found in [31].

This chapter has summarized a method for building realistically-shaped numerical breast models for electromagnetic simulations. The models are derived from MRIs of the breast by segmenting the breast shape from the background, and a thin layer of skin from the breast. In some cases, malignant tissue is also segmented from the surrounding healthy tissue. This process is repeated for each MRI slice. The segmented tissues are transformed into surfaces, and then into solid bodies. Thus, a realistic 3-dimensional solid breast model, including a skin layer, is generated.

Chapter 5 Realistic Experimental Breast Phantoms: Challenges and Solutions

5.1 Introduction to Tissue Phantoms

This chapter presents the construction of realistic experimental breast phantoms for use in validation tests of our microwave imaging system. In order for our phantoms to mimic actual breast tissue as accurately as possible, several tissue types must be incorporated into the breast phantom in such a way that both their dielectric properties and physiological layout approximate those of a real breast. We choose four tissue types that will be incorporated in the breast phantoms: fat, gland, skin and tumor. These tissue phantoms are first mixed individually – and their relative permittivity and conductivity measured – and then they are combined into complete breast phantoms. The aim is to improve on previous phantom work from the literature (Section 2.3) by incorporating all four tissue phantoms into a resulting breast phantom that has a realistically-sized skin layer, gland-like structures surrounded by fat, and that can include tumors of any desired size at any desired location within either the gland or fat phantoms.

The breast phantoms made are hemi-spherical with a radius of 6.5 cm. They include a 2.5-mm layer of skin which is filled in by a combination of fat, gland-like structures and tumors. The phantoms are placed inside the mould in the experimental set-up, with space between the phantom and the mould for a matching medium. The matching medium has the purpose to, in the final system, fill any possible air gaps between the patient's breast and the antenna-containing mould. It will also have impedance-matching properties favorable to antenna performance. The matching medium can be made from either the fat-mimicking phantom or the skin-mimicking phantom [32] and only future experiments with our set-up will determine which is preferable in terms of signal processing.

The next several sections discuss the details of the breast phantom construction [33]. The design of the bowls used in making the 2.5-mm layer of skin phantom is described first. Then, the chemicals and mixing procedure used for each of the four tissue phantoms are presented, followed by the measurements of their respective dielectric properties. Finally, the steps to constructing a complete breast phantom are given. We note that in this chapter, and throughout the thesis whenever in the context of phantom construction, “skin” refers to the skin-mimicking material, and likewise for the other three tissues.

5.2 Design and Fabrication of Skin Bowls

The thickness of skin is variable, with an average thickness of around 2-2.5 mm [30]. This means we need a method of creating a 2.5-mm thick skin phantom around the outside of the breast fat phantom. We decided to have two similar bowls with a 2.5 mm difference in their radii. The smaller one has a radius of 6.25 cm and the larger 6.5 cm. The smaller bowl is solid on the inside, while the larger one must be hollowed (inner radius 6.5 cm). The shape of the outer surface of the large bowl is not important; although a flat bottom is desirable for stability.

The requirements for the bowl material are that it should have very low water absorption (water leaving the skin phantom could adversely affect its dielectric properties) and it should be easy to machine with accuracy and smooth, finished surfaces. The material chosen is Acetal Copolymer. It is chosen over other readily available materials Delrin and aluminum because of its lower porosity and moisture absorbency characteristics.

The two bowls are engineered to have an alignment/extraction plate which will facilitate with centring the smaller bowl within the large one and separating the two once the skin phantom has hardened. The plate has two sets of screw holes, one to fasten the two bowls together and another to slowly push them apart by slowly screwing in the screws at equal locations around the bowls. This ensures that the skin does not tear when the bowls are pulled apart. A photograph of the skin-creating bowls is shown in Figure 5.1, with the bowls in both open and closed position.

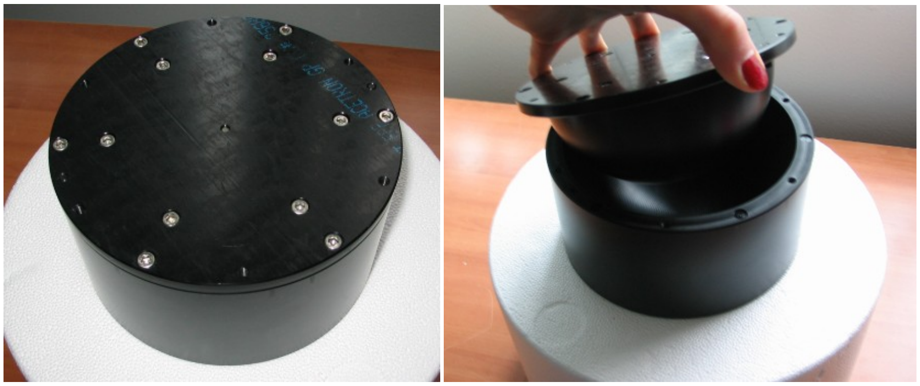

Figure 5.1. Photograph of the bowls used to make the skin phantom: closed (left) and open (right). The solidified material that is poured between the bowls mimics the skin.

A concern with using the skin bowls is that there could be air holes in the skin phantom due to either pouring the liquid into the small space or compressing the liquid by pushing in the small bowl. This can be avoided by pouring the liquid in slowly. Another issue is that the skin may tear as the bowls come apart due to rubbing against a rough surface of the bowl material. It is beneficial to wax either or both of the bowls to make it easier for the skin to detach. Ideally, the small bowl will be pulled off and the skin will rest on the bottom bowl, into which the fat phantom will be poured. Our experience shows that, if done with care, this can be achieved without difficulty.

5.3 Mixture of Tissue Phantoms

The first step towards complete breast phantoms is to make four phantoms (fat, skin, gland and tumor) that have electrical properties in the microwave frequency range that are similar to those of actual breast tissue. The choice of chemicals used in mixing the phantoms must then lead to these desirable dielectric properties; as well, it is preferable that the chemicals be cost-effective, easy to obtain and be stable over long periods of storage time. The chemicals that we use are suggested first in [18]. We adapt the concentrations of each chemical used to attain dielectric properties for the four phantom types that are close to those of the actual tissues. The chemicals, along with their concentrations used in mixing each tissue phantom, are listed in Table 5.1. We note that in the table, and from here on, we will refer to a 50:50 combination of kerosene and safflower oil solely as “oil”. Each recipe makes enough tissue phantom to fill a hemispherical bowl of radius 6.5 cm.

The key ingredients used in mixing the tissue phantoms are the deionized water and the oil. These are the components that most affect a phantom’s dielectric properties. For instance, if we make a phantom with a high oil:water ratio then it will have a low relative permittivity and conductivity. On the other hand, if a low oil:water ratio is mixed, the result is a phantom with dielectric properties on the higher end of the scale. The concentration of oil can be adjusted to obtain any desired relative permittivity or conductivity, so we can easily change the contrast in the dielectric properties of the tissue phantoms. One other chemical whose presence should be described is the Ultra Ivory detergent, which acts to help oil and water combine in a homogeneous manner and is thus very important in phantoms that have high concentrations of oil. The other chemicals used pertain to helping the ingredients mix together, and set and hold their shape, and will not be discussed in any further detail.

Table 5.1. List of ingredients and the amount used for mixing each tissue phantom.

	Amount Used			
	Fat	**Gland**	**Skin**	**Tumor**
p-toluic acid (g)	0. 133	0.253	0.294	0.346
n-propanol (mL)	6.96	12.71	28.69	17.00
deionized water (mL)	132.7	310.0	279.5	328.0
200 Bloom gelatin (g)	24.32	43.27	50.02	58.67
Formaldehyde (37% by weight) (g)	1.53	2.74	3.33	3.72
oil (mL)	265.6	68.0	98.6	38.4
Ultra Ivory detergent (mL)	12.00	6.79	5.86	2.00

Instructions for combining the seven chemicals are the same for each tissue type and are given as follows (these are also adapted from [18]):

1. In a small beaker, add the p-toluic acid into the n-propanol. Heat and stir the mixture until the p-toluic acid is dissolved.
2. Mix the p-toluic acid and n-propanol solution into the deionized water.
3. Add the gelatin to the mixture at room temperature.
4. Cover the beaker tightly with saran wrap and place inside a double boiler.
5. Heat the double boiler until the mixture becomes transparent (near 90°C).
6. Remove the beaker with the mixture in it from the double boiler and place in a cool water bath until the temperature decreases to 50°C.
7. In a separate beaker, mix the oil (50% safflower oil and 50% kerosene) and heat the combination to 50°C.
8. Add the oil to the mixture from step 6. Stir until oil droplets disappear.
9. Add in the Ultra Ivory and stir until the mixture becomes uniform (it will turn white).
10. Cool the mixture to about 40°C.
11. Stir in the formaldehyde.
12. Pour into mould and let solidify.

Once the tissue phantoms are mixed and poured into their moulds, they need to be allowed to solidify. Within a couple hours, the phantoms harden to about 90%; however, before removing them from the moulds one should wait 1 or 2 days to ensure they will hold the desired shape. We also note that the phantoms have a shelf-life of several weeks, but they should be held in saran wrap or an air tight container to prevent dehydration, as it significantly changes their dielectric properties.

5.4 Phantom Dielectric Property Measurements

Once the phantoms solidified, their dielectric properties were tested from 200 MHz to 6 GHz. The complex permittivity for each of the four phantom types was measured at room temperature using an HP 85070B dielectric probe attached to an HP 8753D vector network analyzer. In each case the probe was placed flat on the surface of the phantom during the measurement. A minimum of ten measurements was taken from different locations on each individual tissue phantom, and averaged. In some cases, a few extra measurements were taken from inside the phantom to ensure homogeneity.

After each phantom's complex permittivity is recorded, we can calculate from it the relative permittivity and conductivity at each frequency point. Equation (5.1) shows the complex permittivity in terms of the relative permittivity, ε_r, and conductivity, σ; where ε_0 is the permittivity of free space and ω is the angular frequency as given in equation (5.2). Now, we are able to plot each tissue phantom's relative permittivity and conductivity versus frequency over the microwave frequency range of interest.

$$\varepsilon = \varepsilon' - j\varepsilon'' = \varepsilon_r - j\frac{\sigma}{\omega\varepsilon_0} \tag{5.1}$$

$$\omega = 2\pi f \tag{5.2}$$

The measurement results showing the relative permittivity variation with frequency for the four tissue phantoms are given in Figures 5.2 and 5.3. The results for the gland and fat phantoms are shown in Figure 5.2; also presented on the plot is the median of measurements performed on actual fat and gland tissues from the literature [34]. Figure 5.3 shows the relative permittivity for the skin and tumor phantoms along with the median from measurements of actual skin tissue (from [18], [35]) and actual malignant tissue (from [17]).

Similarly, Figures 5.4 and 5.5 give the conductivity from the measurements for the gland and fat tissue phantoms, and the skin and tumor phantoms, respectively. As with the relative permittivity plots, the conductivity plots also show the median conductivity from actual tissue measurements from the literature for each tissue type [34], [17], [18], [35].

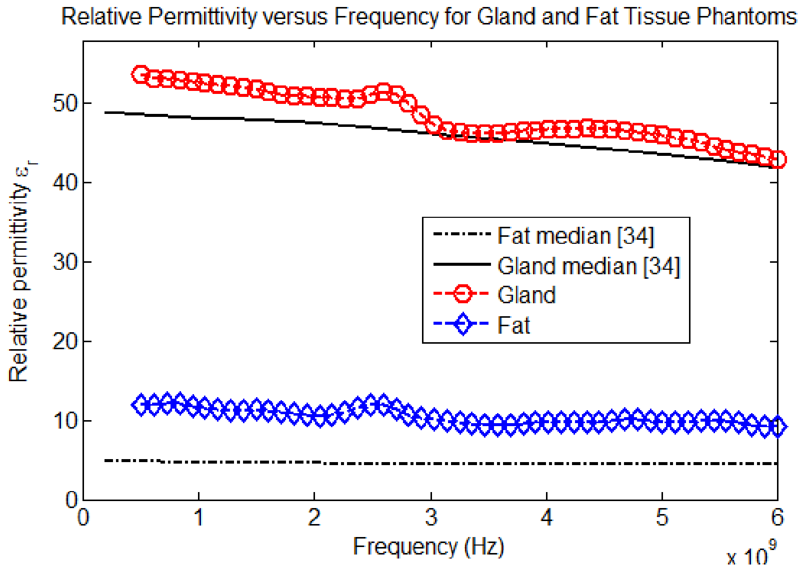

Figure 5.2. Relative permittivity versus frequency for gland and fat tissue phantoms. Also shown is the median relative permittivity of measurements conducted in [34] on actual fat and glandular tissue.

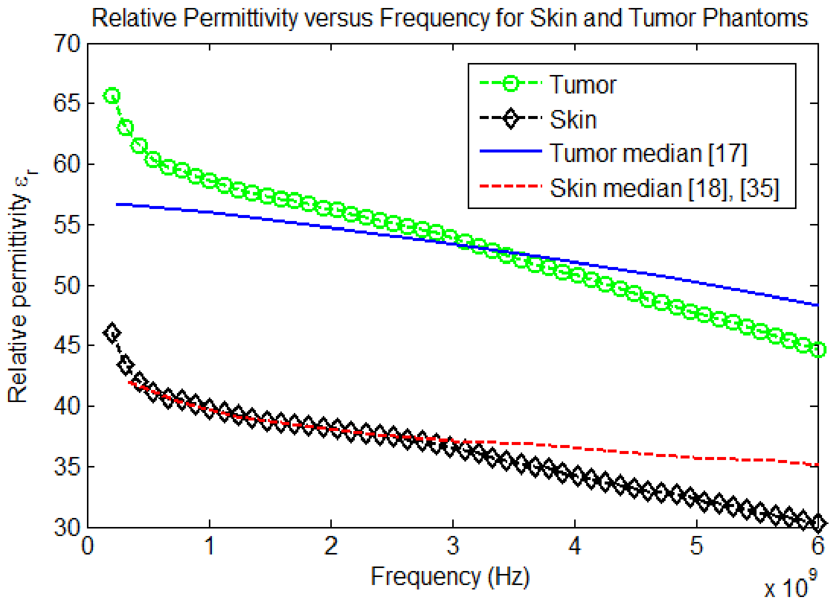

Figure 5.3. Relative permittivity versus frequency for tumor and skin tissue phantoms. Also shown is the median relative permittivity of measurements on actual skin tissue (from [18], [35]) and actual tumor tissue (from [17]).

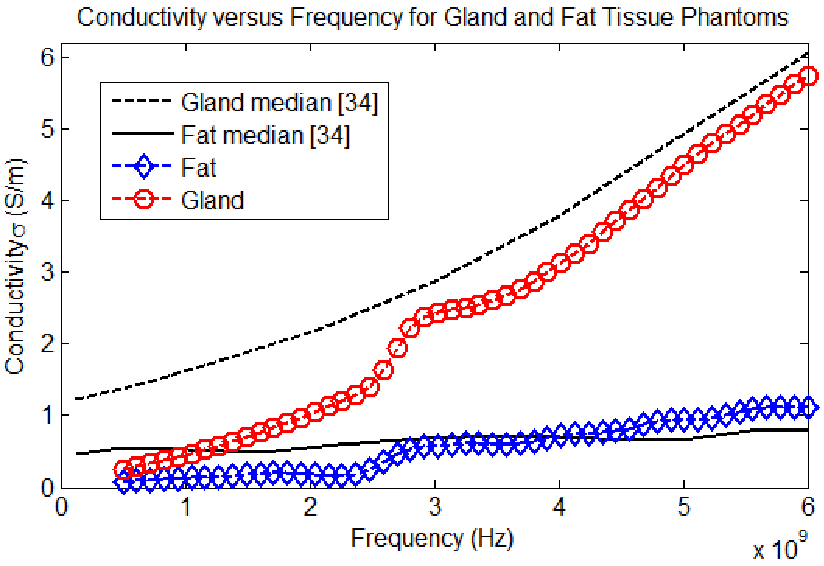

Figure 5.4. Conductivity versus frequency for gland and fat tissue phantoms. Also shown is the median conductivity of measurements conducted in [34] on actual fat and glandular tissue.

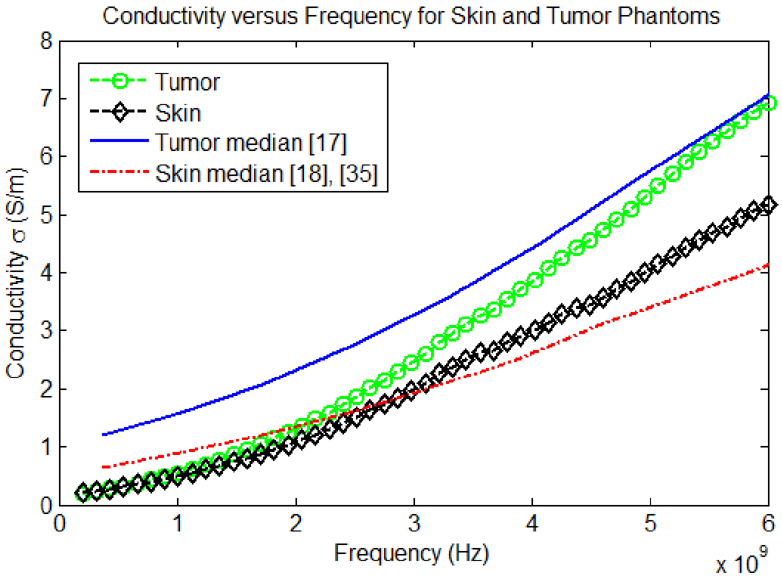

Figure 5.5. Conductivity versus frequency for tumor and skin tissue phantoms. Also shown is the median conductivity of measurements on actual skin tissue (from [18], [35]) and actual tumor tissue (from [17]).

We note that the for the tumor and skin phantoms, the match between our measurements and actual tissue measurements in both relative permittivity and conductivity is good, especially when compared to the intrinsic variations in tissue properties from breast to breast and patient to patient [15]. Our gland phantom's dielectric properties are also near the median reference properties for relative permittivity; however, below 2.5 GHz the conductivity measurements differ from the reference by roughly 1 S/m. Since glandular tissue properties vary so much within the breast and between patients [34] our phantom is still considered to have appropriate properties, especially when we take into consideration the fact that below 2.5 GHz our antenna behaves so poorly that we would only be interested in experiments with frequencies higher than this anyways. The fat phantom, on the other hand, has appropriate conductivity values but a slightly higher relative permittivity as compared to the median of actual fat tissue. We do not believe that the difference in the relative permittivity of the phantom and actual tissue is significant, once again due to intrinsic variations in tissue properties.

It is also important to note that even the most recent actual tissue measurements reported in the literature by no means represent absolutely accurate values that need to be matched unconditionally. In fact, the measurements show high variability in the dielectric properties for all of the tissue types (glandular tissue in particular) [15]. Hence, we aim to have phantoms with properties that are approximate to those of actual tissue. Another factor to have in mind is that the actual tissue measurements were performed on *ex vivo* samples, and as is becoming increasingly apparent, the dielectric properties of tissue could change drastically for the *in vivo* case [7]. Despite these issues, the studies that we reference for actual tissue measurements are the most comprehensive presented to date, and therefore we decided to use them as a guideline for the tissue property values.

Figures 5.6-5.9 give the relative permittivity and conductivity standard deviations in our measurements for the fat, gland, tumor and skin phantoms, respectively. The electrical properties of human tissues themselves have intrinsic variations, so it is natural that our phantoms should exhibit these as well. The differences in successive measurements of the phantom's dielectric properties are not more than actual tissue's inherent variances.

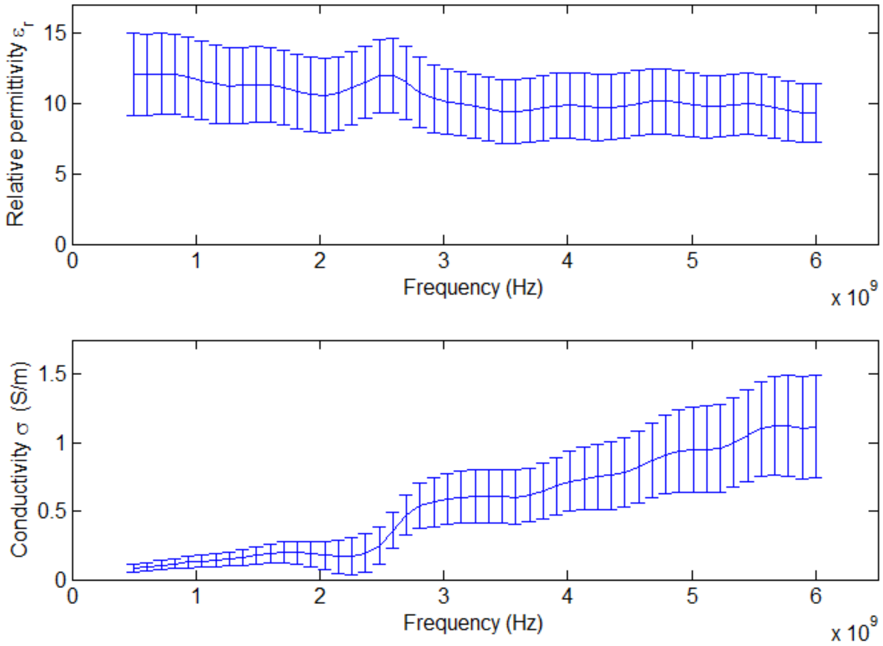

Figure 5.6. Relative permittivity (top) and conductivity (bottom) versus frequency for the fat phantom showing the standard deviation of measurements.

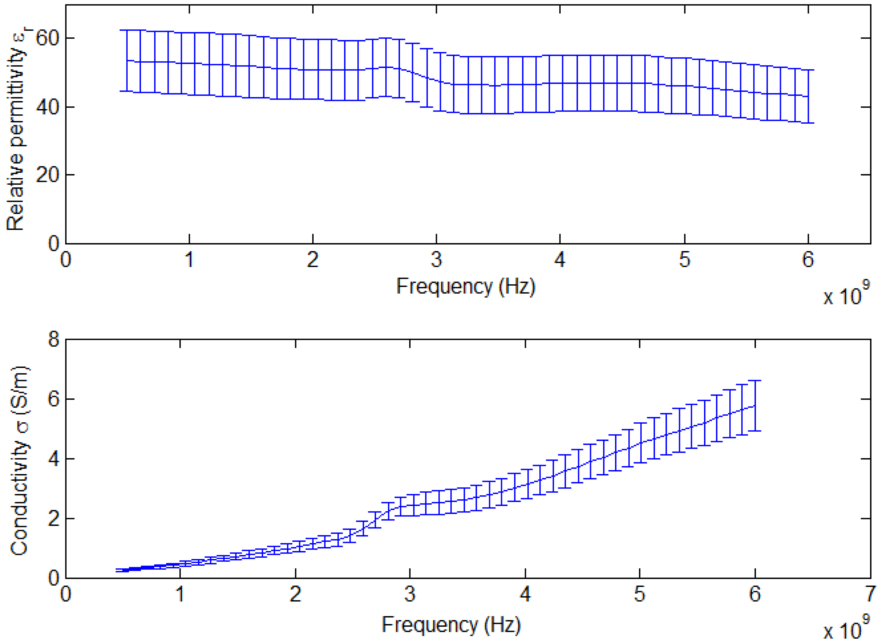

Figure 5.7. Relative permittivity (top) and conductivity (bottom) versus frequency for the gland phantom showing the standard deviation of measurements.

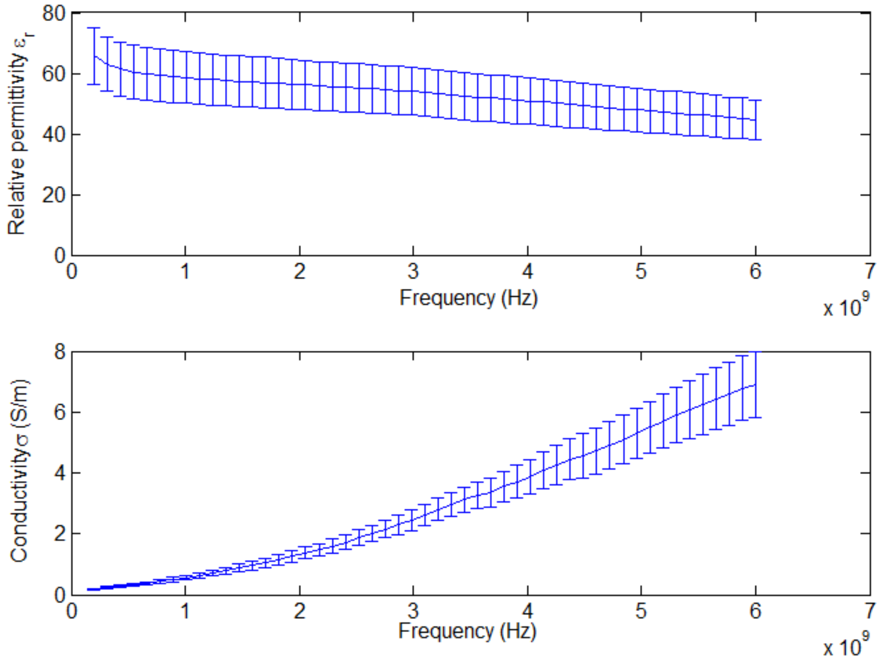

Figure 5.8. Relative permittivity (top) and conductivity (bottom) versus frequency for the tumor phantom showing the standard deviation of measurements.

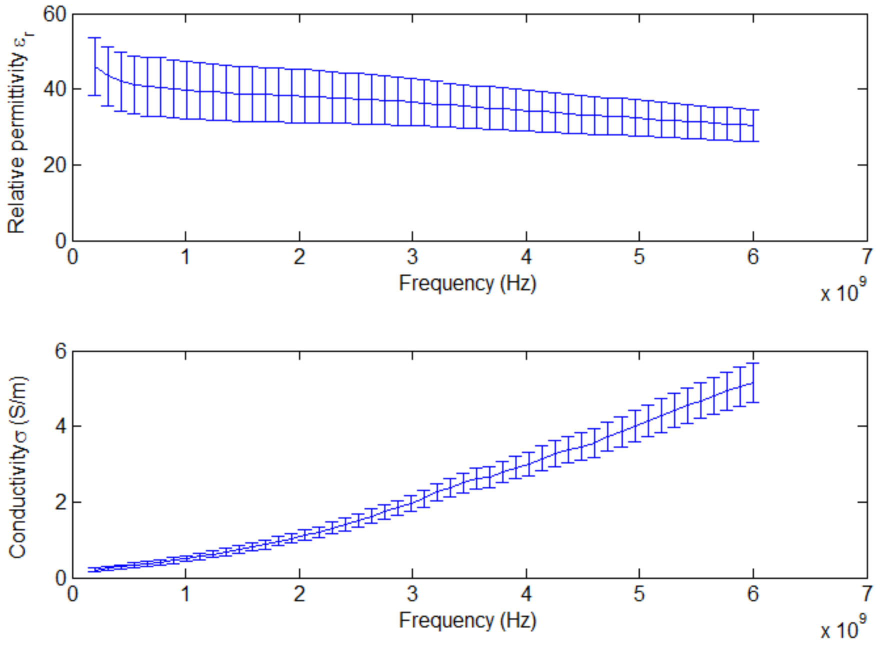

Figure 5.9. Relative permittivity (top) and conductivity (bottom) versus frequency for the skin phantom showing the standard deviation of measurements.

5.5 Construction of Complete Breast Phantom

In this section, we describe how the four tissue-mimicking phantoms can be merged into a model that, geometrically, represents inhomogeneous breast tissue. The first step to making a complete breast phantom is to pour the liquid skin phantom into the skin bowls. Once the mixture has had sufficient time to harden, the skin bowls can be separated. There are some practical challenges associated with this technique of compressing the skin phantom in a small volume between the two bowls. First, it can be difficult to avoid the formation of air pockets within the liquid skin phantom mixture during the compression of the bowls. Secondly, when the two containers are separated, the skin phantom could tear. However, we found that the design of the skin bowl alignment and extraction plates are a big step towards alleviating these challenges. It allows a slow and steady compression of the liquid phantom between the two bowls which prevents the creation of air pockets. Also, by pulling the bowls apart slowly by applying equal pressure on all sides the bowls can be separated without tearing.

Once the skin phantom has hardened and the skin bowls are separated, the fat phantom can be poured directly into the skin-shell. If the complete phantom is to include one or more tumors then a batch of tumor phantom mixture should be made ahead of time and allowed to solidify. Then, the tumor phantom can be easily cut into the desired shape and size. The fat phantom can be poured into the skin-shell in successive layers, enabling the tumor(s) to be placed at any desired location within the fat.

Finally, gland-mimicking tissue can be incorporated into the complete breast phantom. This is done via a slightly more complicated procedure. We note that glands have an approximately conical shape, with the narrower part of the cone being closer to the skin's surface [1], [36]. In order to structurally mimic actual glands, we anchor cylindrical rods in the fat before it solidifies. Once the fat phantom hardens, the rods can be removed and the remaining void can be carved into a conical shape. Then, the gland mixture can be poured directly into the conical hole. This technique permits the inclusion of multiple gland models, as well as for tumors to be placed within the glands by pouring the gland phantom in successive layers.

Figure 5.10 shows an example of a complete breast phantom. It includes phantoms of all four tissue types: skin, fat, gland and tumor. The complete phantom has a radius of 6.5 cm. It has two different glandular structures, a small one and a larger one that contains a 1.5-cm tumor.

Figure 5.10. Photograph of a complete breast phantom including skin, fat, glands and tumor.

Chapter 6 Antenna Design, Simulations and Measurements

6.1 Antenna Design and Characteristics

Microwave radar imaging of the breast requires a broadband antenna to transmit an ultra wideband pulse and receive the signals. Considering the application, the antenna chosen should be small in size (on the order of a couple centimetres) and have a good quality radiated beam in the forward direction for the frequency band of interest [37]. Two types of designs have been published, either using variable or constant surface resistive loading. Variable resistive loading was the original method for broadband antenna design, but constant resistive loading has the potential to provide good antenna behaviour while being more practical and cost-effective [38].

The antenna considered in our simulations and experiments is one that was designed by H. Kanj [39], [40]. It is called the Traveling Wave Tapered and Loaded Transmission Line Antenna (TWTLTLA) and was designed specifically for broadband applications. The antenna has been adapted from the “Dark Eyes” antenna via several slight alterations [39]. It is planar and designed using constant resistive loading. The antenna is formed using a tapered transmission line, in this case with characteristic impedance of 50 Ω, with resistively loaded “eyes” that can be built to have a conductivity, σ, of 2285.7 S/m, 1142.8 S/m, 571.4 S/m or 285.7 S/m (that is, surface resistivity R_s of 25 Ω/square, 50 Ω/square, 100 Ω/square and 200 Ω/square, respectively). The resistive loading reduces the amount of reflections off the end of the antenna. Also, the smooth edges of the “eyes” lead to input impedances that change more smoothly with frequency, which is why smooth edges are usually employed in broadband antenna designs [10]. The TWTLTLA also has very good signal fidelity (above 0.95), and a radiation efficiency of 39.21% for R_s = 50 Ω/square [39]. The antenna operates best in a medium with dielectric constant ε_r = 10.2, which matches the dielectric constant of the antenna substrate [39]. An image of the antenna is shown in Figure 6.1; this particular one has R_s = 200 Ω/square. The antenna itself has dimensions of only 0.635 x 12 x 15.8 mm^3.

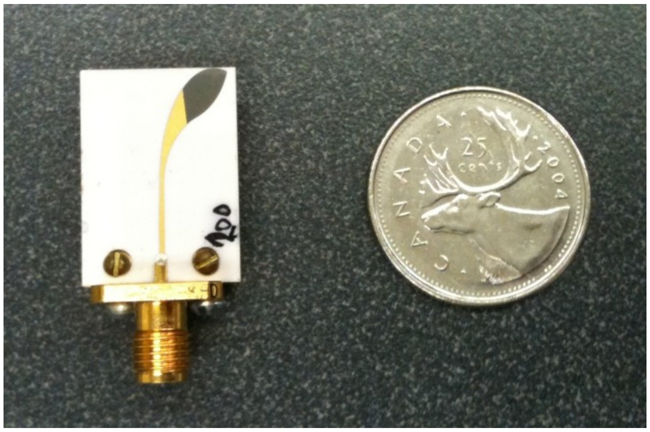

Figure 6.1. The TWTLTLA with R_s = 200 Ω/square shown next to a quarter for scale.

This chapter presents simulations and measurements of the return loss, S_{11}, of the antenna under various circumstances. The S_{11} parameter is of particular interest for our application given that excessive reflections from the end of the antenna can obscure the desired (tumor response) signal. Since the Federal Communications Commission (FCC) in the United States limits the bandwidth of medical equipment to between 3.1 and 10.6 GHz [41], this will be our frequency range of interest and for this band we will require an S_{11} of -10 dB or less. The S_{11} resulting from the antenna placed in air, a fat-like medium and a suitcase inside the mould is reported in the next three sections. All simulations and measurements are done for all four surface resistivities under investigation.

6.2 Antenna S_{11} Simulations and Measurements in Air

The antenna's return loss is initially tested in air. Of course, in the final experimental set-up the antenna should have no air around it, but knowing the behaviour in air is a good reference point. Firstly, the antenna is simulated using SEMCAD-X, with the background medium set to air (i.e., ε_r = 1 and σ = 0). A source is placed at the base of the antenna which simulates a Gaussian pulse excitation. Upon completion of the simulation, the S_{11} parameter is plotted. This process is repeated four times, varying R_s to equal 25 Ω/square, 50 Ω/square, 100 Ω/square and 200 Ω/square.

Figure 6.2 shows the graph of the simulated return loss in air versus frequency for each of the possible antenna surface resistivities. It is noted that over the 3.1 – 10.6 GHz frequency band the results are poor for all four simulations. However, at higher frequencies all the antennas perform better, in particular the one with R_s = 25 Ω/square, which has S_{11} < -10 dB from 7.25 GHz all the way up to 20.05 GHz. The antenna simulation with R_s = 50 Ω/square exhibits similar but slightly degraded behaviour compared to the R_s = 25 Ω/square case; further, it is seen that R_s = 200 Ω/square leads to a very poor return loss characteristic. Hence we conclude that over the 0 to 36 GHz frequency range, a higher surface resistivity leads to overall inferior antenna performance.

Next, each of the four antennas characteristics were measured in free space. The antennas were connected to the input port of a vector network analyzer (Agilent 8703B Lightwave Component Analyzer), set to measure electrical parameters. A frequency sweep from 50 MHz to 18 GHz was performed. At each of 1601 frequency points, S_{11} was measured and saved. The results of these measurements are shown in Figure 6.3.

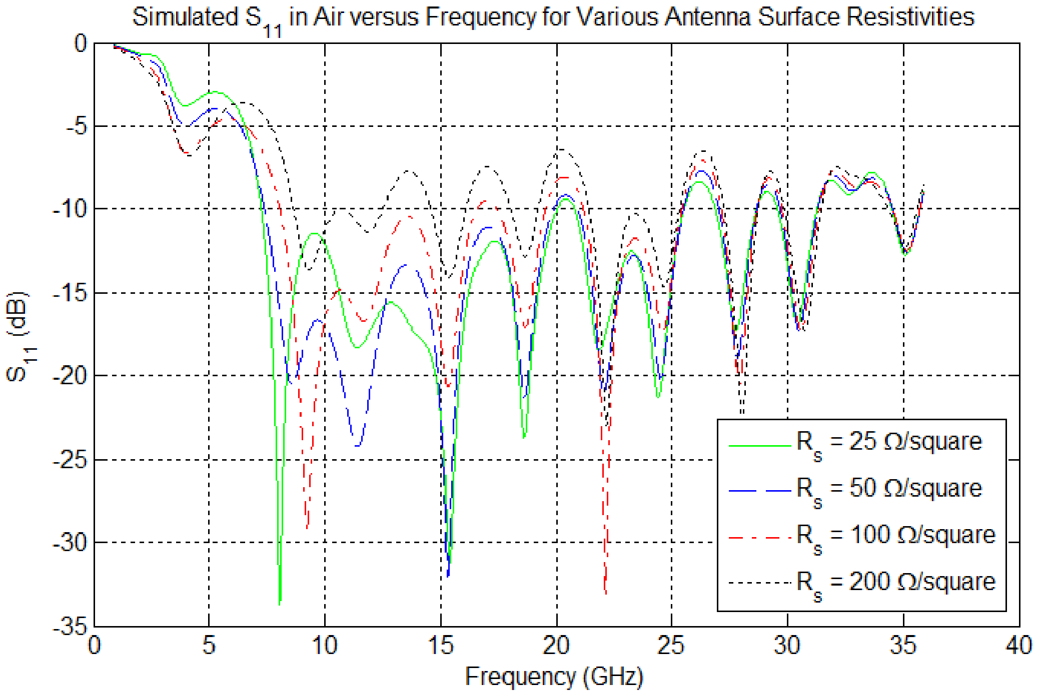

Figure 6.2. Plot of the simulated return loss in air versus frequency for four different antenna surface resistivities.

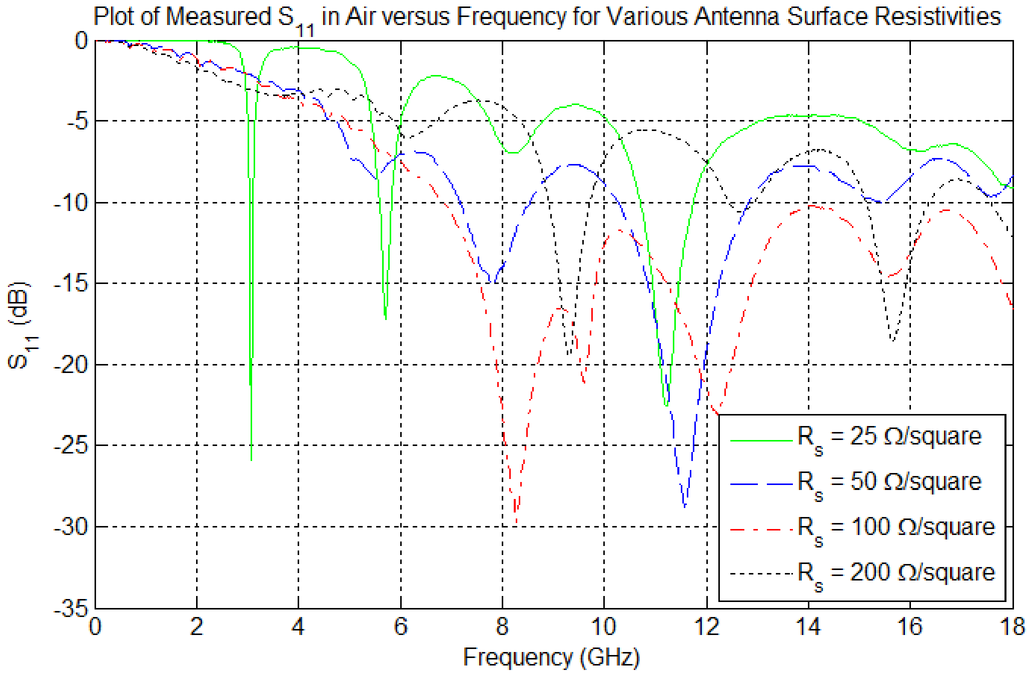

Figure 6.3. Plot of the measured return loss in air versus frequency for four different antenna surface resistivities.

A final set of measurements was performed using eight 50 Ω/square antennas in air. The measurements were done using the same procedure as in the previous paragraph, with the exception that the frequency sweep was increased to 20.05 GHz. The purpose of this set of measurements was to verify whether or not all of the 50 Ω/square antennas had similar properties. The return loss for the eight antennas is shown in Figure 6.4. Seven out of the eight antennas have very similar return loss characteristics; however one, shown with the solid blue line on the plot, clearly behaves differently than the others. This is attributed to flaws or damage done during the manufacturing process, and for this reason this particular antenna will not be included in any further measurements.

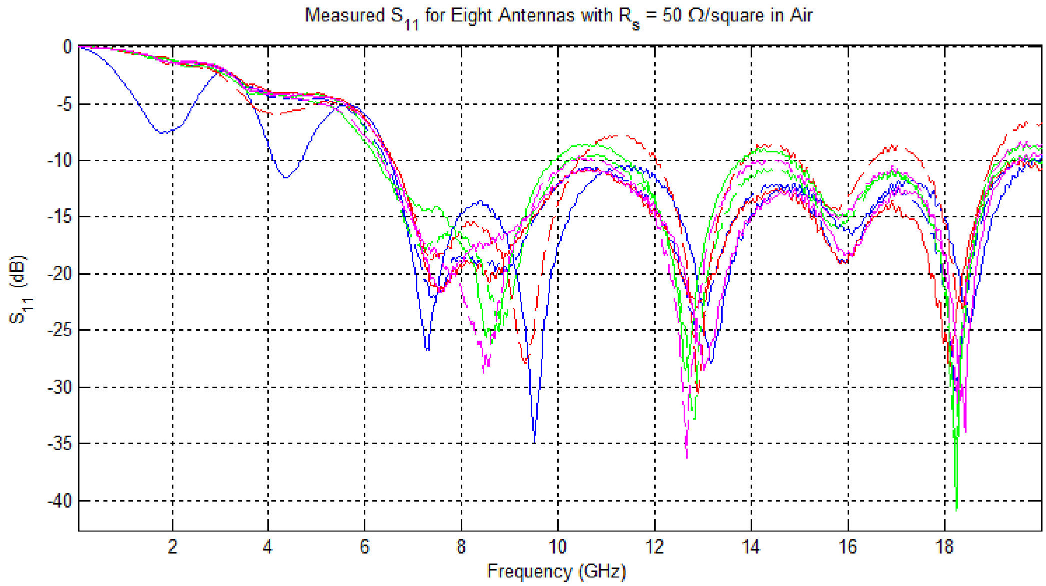

Figure 6.4. Plot of the measured return loss in air versus frequency for eight different 50 Ω/square antennas.

6.3 Antenna S_{11} Simulations and Measurements in Fat-like Medium

In this section, the return loss of the TWTLTLA in a fat-mimicking medium is investigated. Simulations are performed in the same manner as in 6.2; however, the antenna is now immersed in a fat-like medium instead of in air. Since the antenna is built to have best performance in a medium with ε_r = 10.2, which is close to that of fat, we expect the results seen in this set of tests to be better than those from section 6.1. The fat-like medium used has a relative permittivity ε_r = 9.92 and a conductivity σ = 0.4 S/m.

Figure 6.5 plots the simulated S_{11} for each surface resistivity. As can be observed, the return loss is below -10 dB from 1.58 GHz to 25.3 GHz in the R_s = 25 Ω/square case and from 1.33 GHz to 19.1 GHz with R_s = 50 Ω/square. Both of these fit the criteria of having S_{11} < -10 dB from 3.1 to 10.6 GHz. The higher surface resistivity antennas, however, show a peak in S_{11} near the centre of our frequency of interest, and hence are not, for our purpose, acceptable options.

The return loss is measured for each antenna when it is immersed in a fat-approximating phantom. The measurements are taken with the VNA using the same method described in Section 6.2, except by placing the antenna (up to the connector) into the fat phantom. The description and summary of the electrical properties of this fat-like medium can be found in Chapter 5. The resulting S_{11} measurements are given in Figure 6.6. The antenna with the best return loss over the desired frequency range is the one with R_s = 50 Ω/square, followed by R_s = 100 Ω/square. The simulated and measured data likely differ because of the fat-like medium's electrical properties. For instance, the relative permittivity and conductivity of the phantom are not exactly the same as those used in simulations, and also vary with frequency. Another source of error is the likelihood that there exist small air gaps between the antenna and the fat phantom that could adversely affect the measurements.

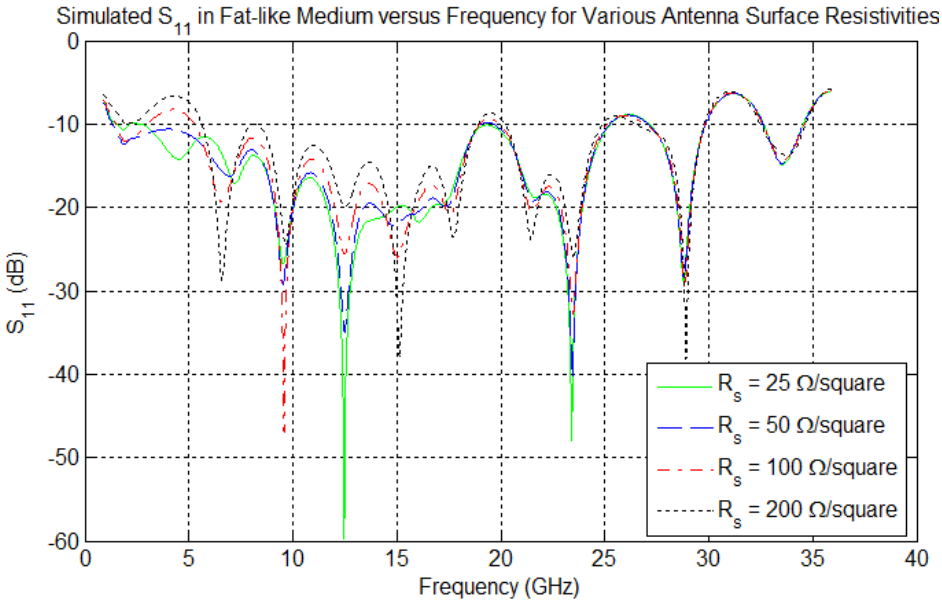

Figure 6.5. Plot of the simulated return loss in a fat-like medium versus frequency for four different antenna surface resistivities.

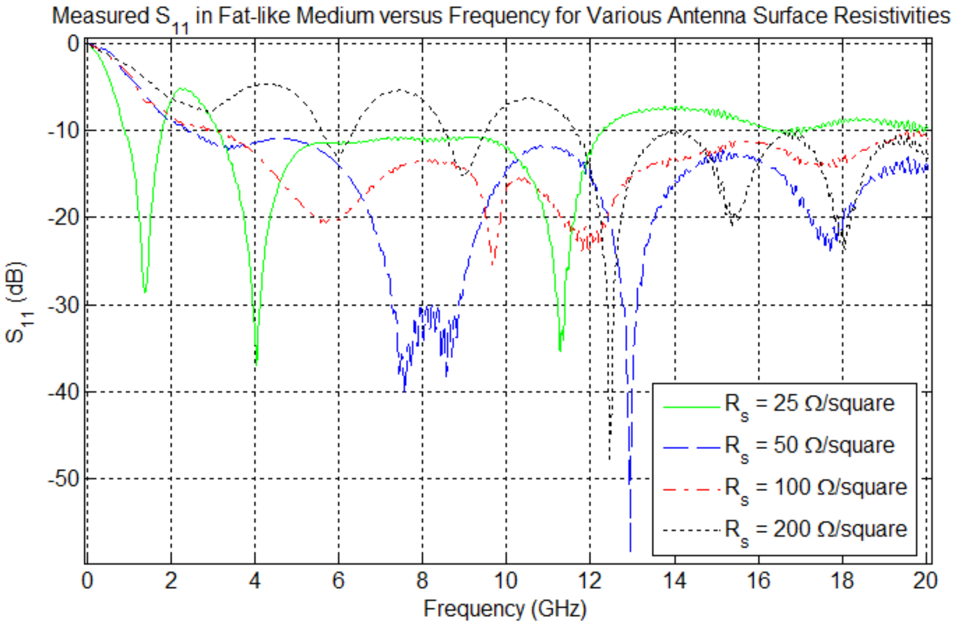

Figure 6.6. Plot of the measured return loss in a fat-like medium versus frequency for four different antenna surface resistivities.

Return-loss measurements were also taken on a set of eight 50 Ω/square antennas, to verify the consistency of their behaviour. The plot of measured S_{11} values for each of the eight antennas is shown in Figure 6.7. The antenna represented by the solid blue line on the graph was already noted in Section 6.2 to have unexpected properties; the same discrepancy is noticed here and thus this antenna is discarded. The other seven antennas have return loss characteristics in the fat-like medium that are relatively close to each other. Small differences between them can be accounted for by the following facts: any small air gaps between the antenna and the fat-like medium are variable from measurement to measurement and would change the S_{11} parameter, and, the fat-like medium has dielectric properties that differ slightly from location to location within the medium. Thus antennas positioned at different locations within the fat-like medium would experience different return losses.

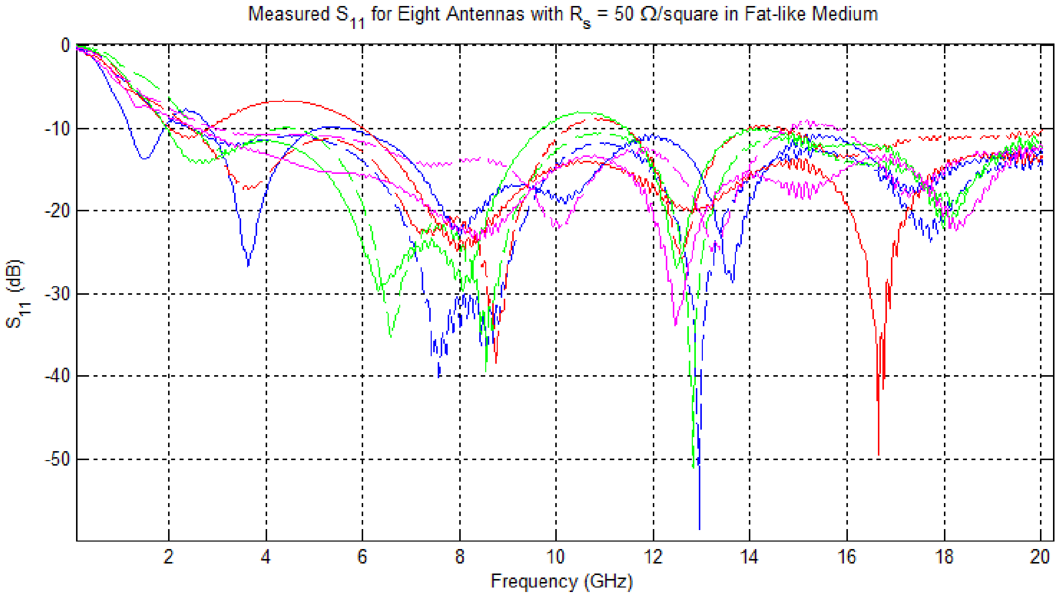

Figure 6.7. Plot of the measured return loss in a fat-like medium versus frequency for eight different 50 Ω/square antennas.

6.4 Antenna S_{11} Simulations and Measurements in "Suitcase" in Mould

A final set of simulations and measurements are performed on what would be the actual experimental set-up. In each of these simulations, the antenna is placed in a suitcase-like holder (ε_r = 10), and the suitcase itself is placed in the mould (ε_r = 9.6). The suitcase has dimensions 3 mm x 18 mm x 12 mm, and the antenna fits snugly inside it with only a 1-mm strip of suitcase material between the tip of the antenna and the mould (see Chapter 7 for more details about the mould and suitcases). These simulations are ideal, meaning that there are no air gaps between the antenna and the suitcase or the suitcase and the mould (in the corresponding measurements and the actual experiment this will not be the case).

The resulting return losses are shown in Figure 6.8. For each surface resistivity, the S_{11} found here matches closely with the simulated behaviour in fat-like material in Figure 6.5. This is due to the fact that the relative permittivities of the fat-like material and the suitcases with mould are similar. It is also noted that, as expected, there is a slight increase in S_{11} for the suitcase and mould situation since there are more interfaces and therefore more reflections. Out of the four possible surface resistivities, R_s = 50 Ω/square is the only one which satisfies the required criterion, with S_{11} decreasing below -10 dB at 2.59 GHz and only increasing above this limit at 18.8 GHz. However, R_s = 25 Ω/square is acceptable, with S_{11} < -10 dB over the range 3.18 GHz to 18.9 GHz; and thus could also be used in a complete microwave radar imaging system.

Measurements of the same scenario were also performed. The antenna being used is placed inside a suitcase, which is then placed inside the mould. For this series of measurements the procedure used is the same as in Sections 6.2 and 6.3. It is important to note that there are air gaps induced in the set-up which have a negative affect on the return loss parameter. There are perhaps slight air gaps between the suitcase and mould, although every effort in design and manufacture was made to minimize said air-gaps. The major sources of air gaps are between the fat phantom (which fills the mould, but cannot be guaranteed to be airtight) and between the antenna and the suitcase (which fits the antenna tightly on the sides but produces a small space near the tip).

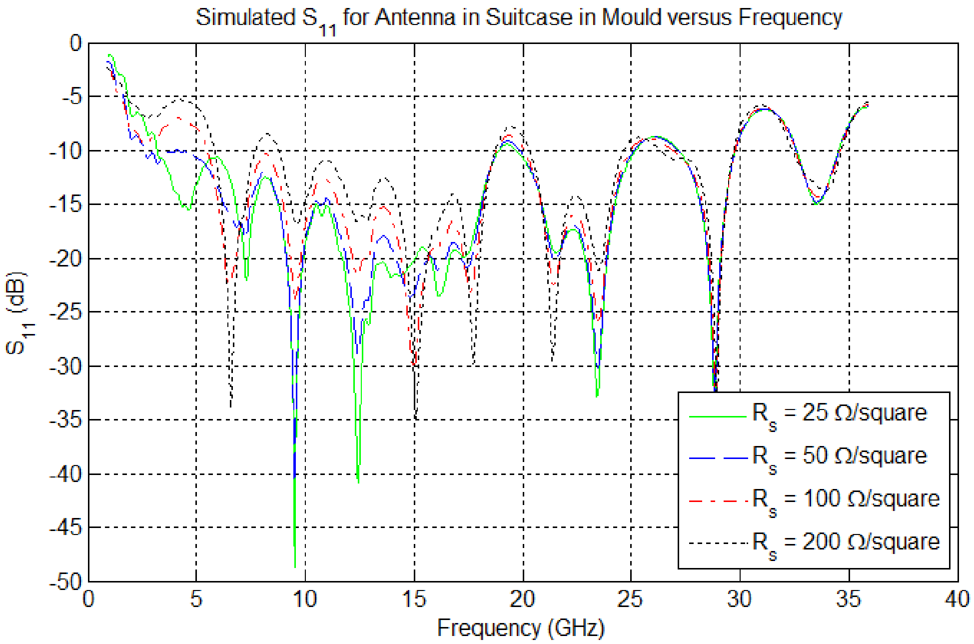

Figure 6.8. Plot of the simulated return loss for antenna in suitcase in mould versus frequency for four different antenna surface resistivities.

The measured S_{11} is shown in Figure 6.9, for each of the four antennas. The antenna with surface resistivity of 100 Ω/square produces the best results, with an S_{11} below or close to -10 dB from about 3 GHz to 13 GHz. The 50 Ω/square antenna shows acceptable results, while the 25 Ω/square one performs poorly. These measurements differ from the simulated values mainly due to the effect of the air gaps mentioned in the previous paragraph.

The 25 Ω/square exhibits a particularly poor S_{11} characteristic in the mould (seen in Figure 6.9), as it did also in Figure 6.6 and Figure 6.3 when immersed in the fat-like medium and air, respectively. In the simulations, the 25 Ω/square antenna had markedly better performance. Since its behaviour is consistently poor, we attribute this to faults in antenna manufacturing. In fact, it was noted that the contact between the antenna feed and the SMA connector is unstable, such that wiggling the antenna leads to visibly huge differences in the return loss being measured.

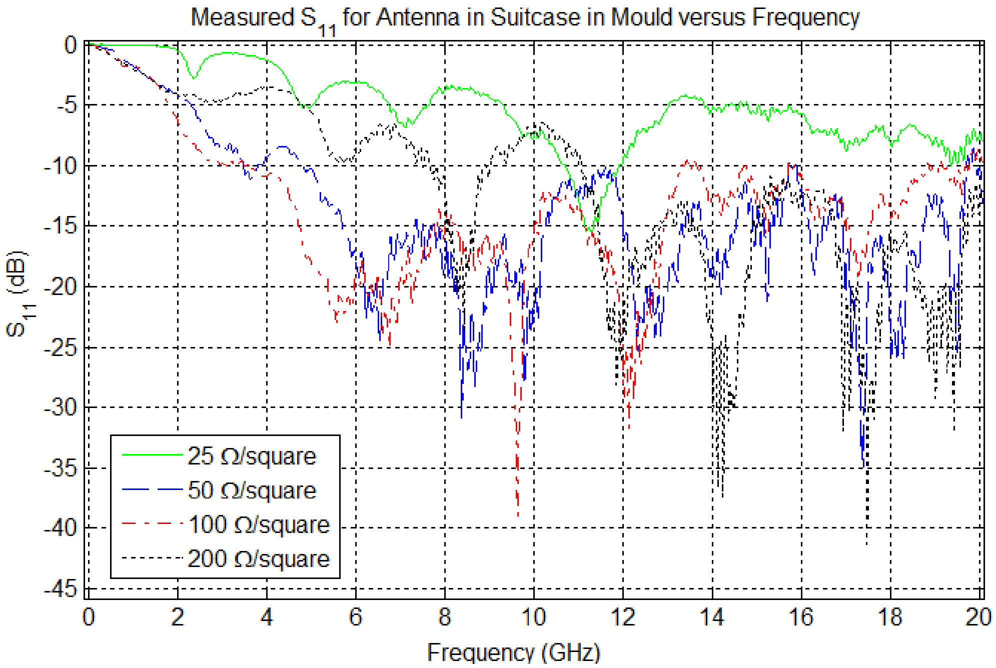

Figure 6.9. Plot of the measured return loss for antenna in suitcase in mould versus frequency for four different antenna surface resistivities.

For the reasons given, the 25 Ω/square antenna will not be chosen for use in the complete imaging system. The 100 Ω/square antenna has the lowest measured S_{11} in the mould over the desired frequency range. The 50 Ω/square antennas have the advantages of having the best performance in the fat-like medium, acceptable performance in the mould and are the easiest to mass-fabricate. Hence, we plan to use them in the final prototype.

Chapter 7 Discussion of Selected Hardware Components

7.1 Introduction to the Mould

A key component of the suggested experimental system is a piece we call 'the mould'. The mould is, in fact, a radome, or antenna holder, that is in the shape of a rigid, hemispherical bra cup. The idea is that the mould will hold in place both the transmitting and receiving antennas on its exterior surface; and the breast (or in this work, the breast phantom) will be placed against the interior surface of the radome cup. The mould is designed specifically for this purpose, with the goal that eventually a similar component, possibly flexible, can be worn by a woman like a bra.

The design of the mould is very important as it will have a direct impact on the quality of the signals obtained. Since it is essential to minimize attenuation over the signal paths, the mould should be made of a material that has very low loss over the microwave frequencies. Another key factor is to decrease the return loss from the antennas as much as possible. This occurs when the material in front of the antenna has a relative permittivity close to 10.2, which matches the relative permittivity of the antenna substrate.

The average breast size for a woman is a B cup, which indicates a hemi-spherically-shaped breast diameter between 14 and 16 centimetres. Taking this into consideration, while retaining a relatively simple, straight-forward experimental procedure, the fat phantoms are chosen to have a diameter of 12.5 cm with an additional 2.5-mm thick layer of skin. This leads us then, allowing a 5-mm space for matching gel (or a slightly larger breast phantom), to a hemispherical bowl-shaped mould that has an inner radius of 7 cm and an outer radius of 8.5 cm. The thickness of the mould permits an antenna to be fully embedded in it up to the connector, leaving a 3-mm section of mould between the tip of the antenna and the matching medium. This 3-mm section is large enough that the mould is not fragile and small enough that the signals are not significantly attenuated when passing through it.

Thus we must find a material for the mould to be fabricated from that is a low loss dielectric and has a relative permittivity as close as possible to 10.2. Through the rest of this chapter, an investigation of several possible mould materials will be performed, followed by a discussion of the parameters of size, shape and the number of antenna slots. The final chosen design for the mould will then be presented.

7.2 Possible Materials for Fabricating Mould

As described in Section 7.1, the mould should be made from a material that has a relative permittivity close to 10.2 and is low loss. Upon further thought, the material should also have very low moisture or water absorption, and must be easy to machine as the antenna slots will be quite small and could present a challenge for some materials. Since the mould has a diameter of 17 cm, the raw material required will be at least 17.4 cm in diameter to allow for smoothing out of roughness during machining. Similarly, the height of the raw material needs to be 8.9 cm. It is also desirable to have a return loss, S_{11}, characteristic for the antenna that is less than -10 dB from at least 3-10 GHz. With these multiple requirements in mind, the next several paragraphs will discuss four materials that were explored for use in fabricating the mould.

The first option considered is a material called HiK, sold by Emerson & Cuming. For this material, the relative permittivity can be chosen (from a range of available values), so in our case, ε_r = 10 could be obtained. It also has a loss tangent $\tan\delta < 0.002$, which suits our low loss requirement. HiK has low water absorption and is easy to machine. However, after many discussions with company representatives, it was determined that the material cannot be shaped into a size as large as needed for the mould without structural instability. Also, the drilling of the slots could cause the material to further crack or fracture. The material is still relatively new, and they expect improvements within the next few years. However, for now, this material was determined to be unusable and other options were explored.

The next possibility for the mould material was Lexan (polycarbonate). Before investigating the properties of this material, we already know that it is widely available in all sizes and it is very easy to machine, two key factors. Upon further research, Lexan is found to have a relative permittivity of 4.4 at 1 kHz, with low loss and low water absorption. Hence the only downside is the low dielectric constant. This may increase the mismatch between the antenna and the mould medium and lead to poor performance, particularly at lower frequencies. We also note that the dielectric constant of Lexan could decrease to about 4.1 as frequency increases, exacerbating the mismatch (however at higher frequencies the return loss of the antenna is low enough that this may not have too much of an adverse affect).

Another material that was researched was Mycalex (machining grade 500), a glass-bonded-mica, made by the company Crystex. At 1 MHz, it has ε_r = 6.9 and tanδ = 0.009. It has no moisture absorption and is also easy to machine and mould. Two difficulties with using this material were identified. Firstly, the low dielectric constant of Mycalex leads to a poor return loss at low frequencies. Secondly, after requesting a quote from the company, it was determined that they would not be able to fabricate it since the bowl of the mould is too thick for it to be made from flat Mycalex stock. Thus fabrication using this material could be difficult, and may require adjustments to the mould size.

The final material investigated for fabricating the mould out of is called Alumina, and is sold by Friatec. Alumina (Al_2O_3) has ε_r = 9.6 at 1 GHz for a sample that has at least 99.5% purity. It has a loss tangent of 5×10^{-4} at 1 GHz and 0% water absorption. Since this material's relative permittivity is higher, the S_{11} performance was anticipated to be desirable at low frequencies.

Having identified several potential materials, simulations were performed with an antenna immersed in a medium with properties matching those of the possible materials. The S_{11} characteristics were plotted up to 35 GHz. The material we ultimately choose will be one that has the best S_{11} over the frequency range of interest for our work, namely from 3-10 GHz. So simulations for three materials (Lexan, Mycalex and Alumina) will be presented; HiK was not included in the simulations due to its fragility.

Figure 7.1 represents the ideal case – the antenna is immersed in a medium that has a relative permittivity equal to 10.2. The simulated return loss is shown for each of the four possible antenna surface resistivities: 25 Ω/square, 50 Ω/square, 100 Ω/square and 200 Ω/square. In this case we see both the 25 Ω/square and the 50 Ω/square antennas have acceptable return loss at low frequencies. This ideal case will be a useful comparison for the actual material types – the closer the antennas' behaviour in the material is to the ideal case, the better.

Figures 7.2 and 7.3 show the return loss for antennas immersed in Lexan (ε_r = 4.4) and Mycalex (ε_r = 6.9), respectively. In both cases we note that the 50 Ω/square antenna has the best performance, however we see a significant degradation as compared to the ideal case. The performance is worse for the ε_r = 4.4 case than for ε_r = 6.9, as would be expected. Finally, Figure 7.4 gives the simulated return loss for each of the antennas immersed in a medium with relative permittivity of 9.6 (that of Alumina). This time the results are much closer to the ideal case, and both the 25 Ω/square and 50 Ω/square antennas

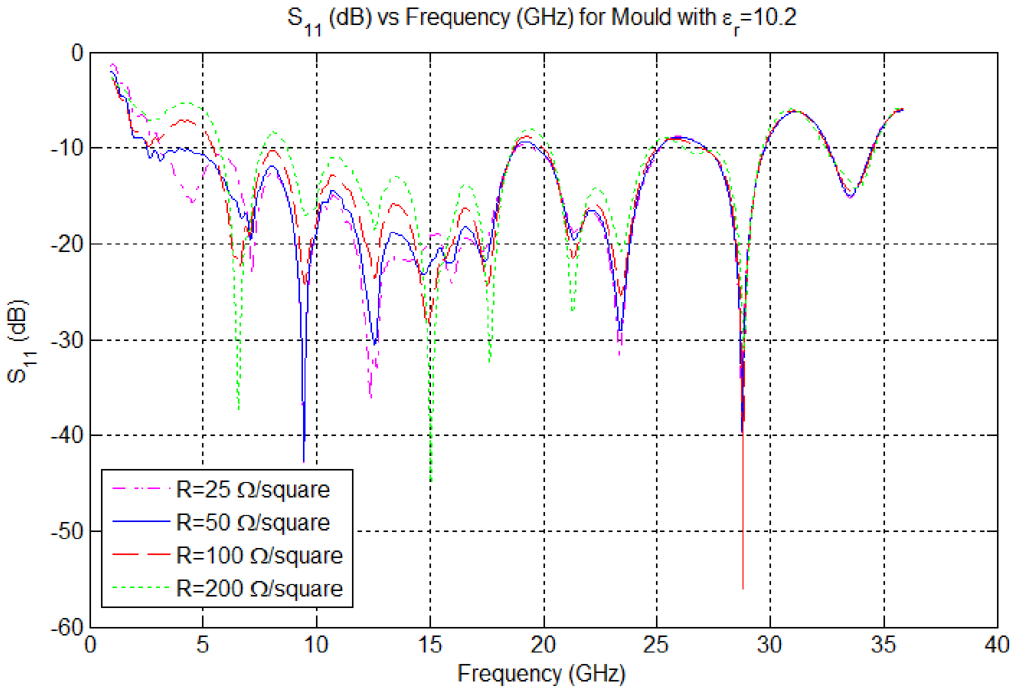

Figure 7.1. Plot of the simulated return loss versus frequency for four antennas immersed individually in a medium with relative permittivity of 10.2.

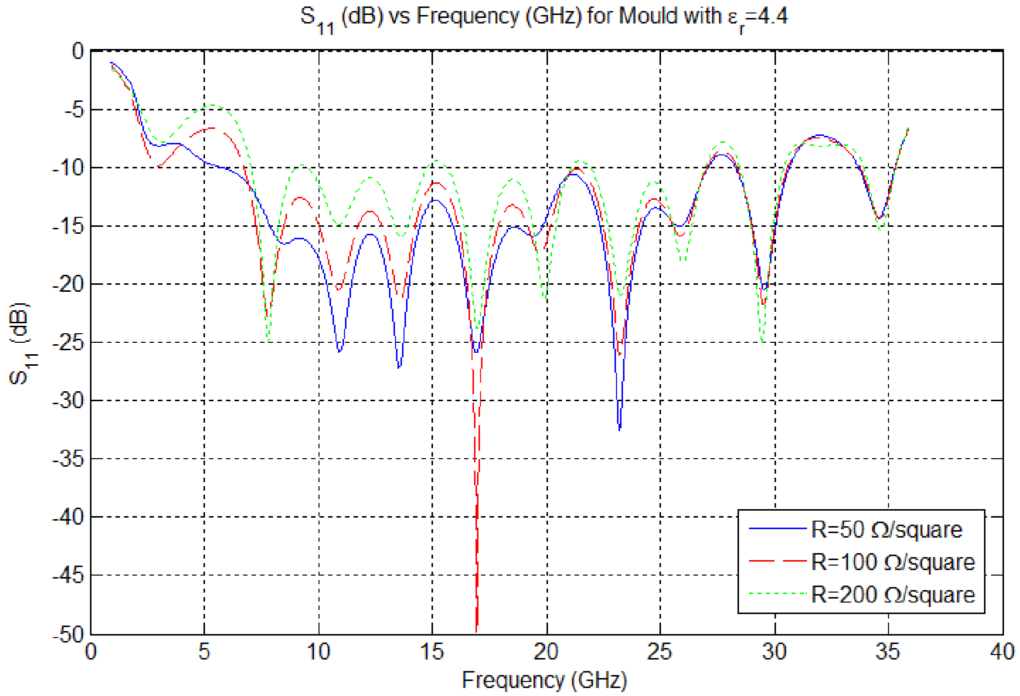

Figure 7.2. Plot of the simulated return loss versus frequency for three antennas immersed in a medium with relative permittivity of 4.4 (Lexan).

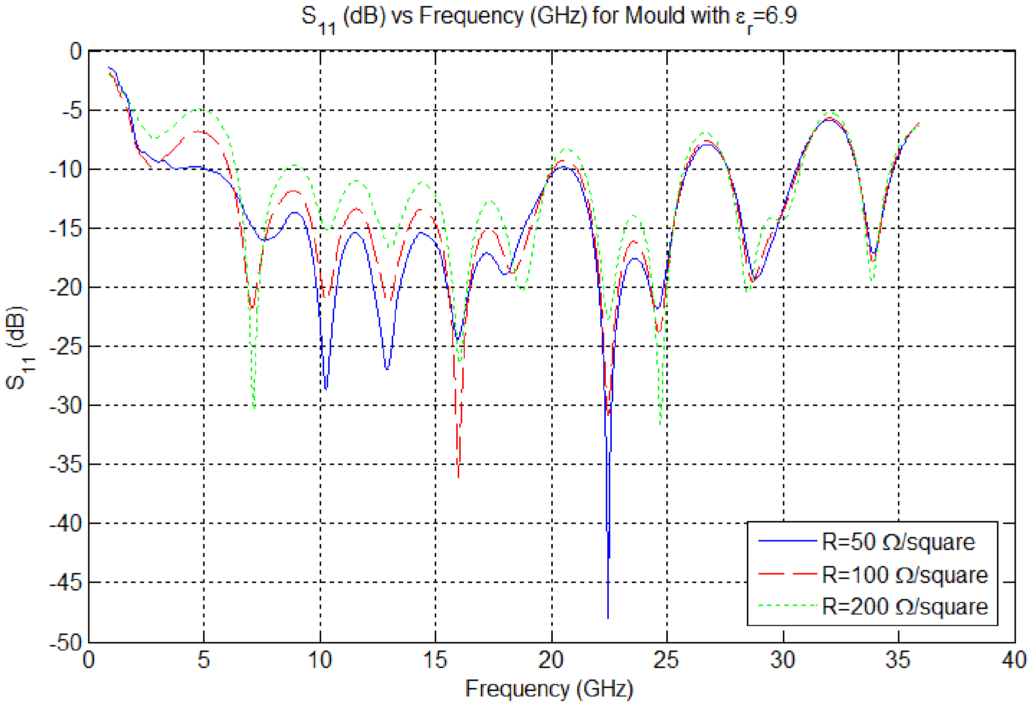

Figure 7.3. Plot of the simulated return loss versus frequency for three antennas immersed in a medium with relative permittivity of 6.9 (Mycalex).

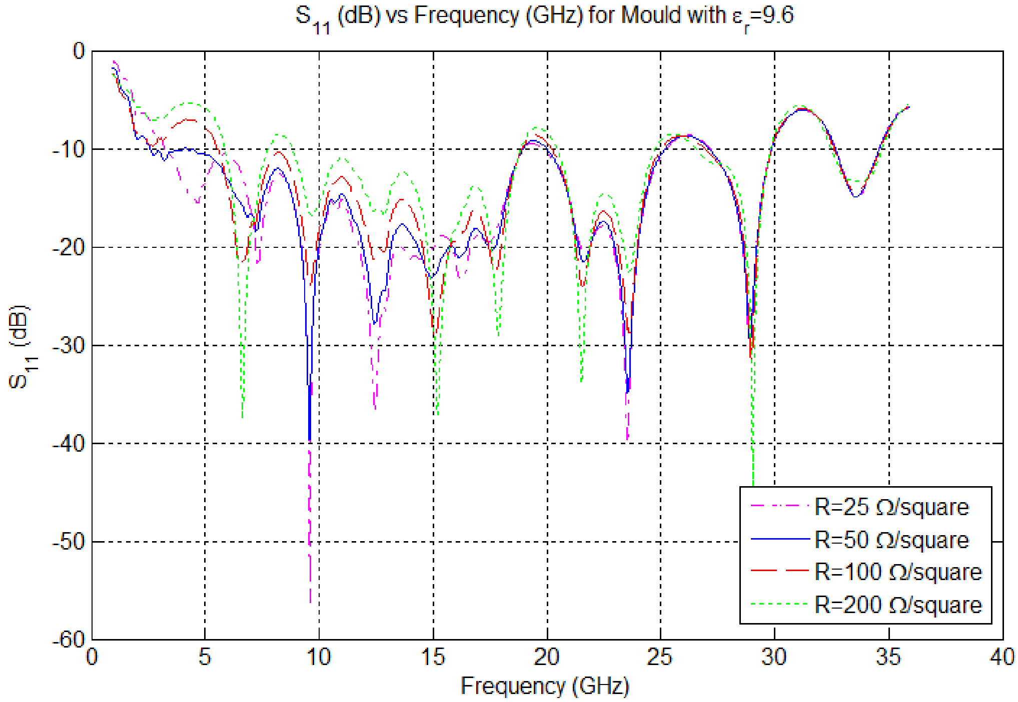

Figure 7.4. Plot of the simulated return loss versus frequency for four antennas immersed in a medium with relative permittivity of 9.6 (Alumina).

exhibit good characteristics. In fact, a direct comparison between Alumina and the ideal mould material is shown in Figure 7.5 for the 50 Ω/square antenna (the antenna that was already seen in Chapter 6 to have the better performance). The differences between the return losses of the two are insignificant, especially at the lower frequencies of concern.

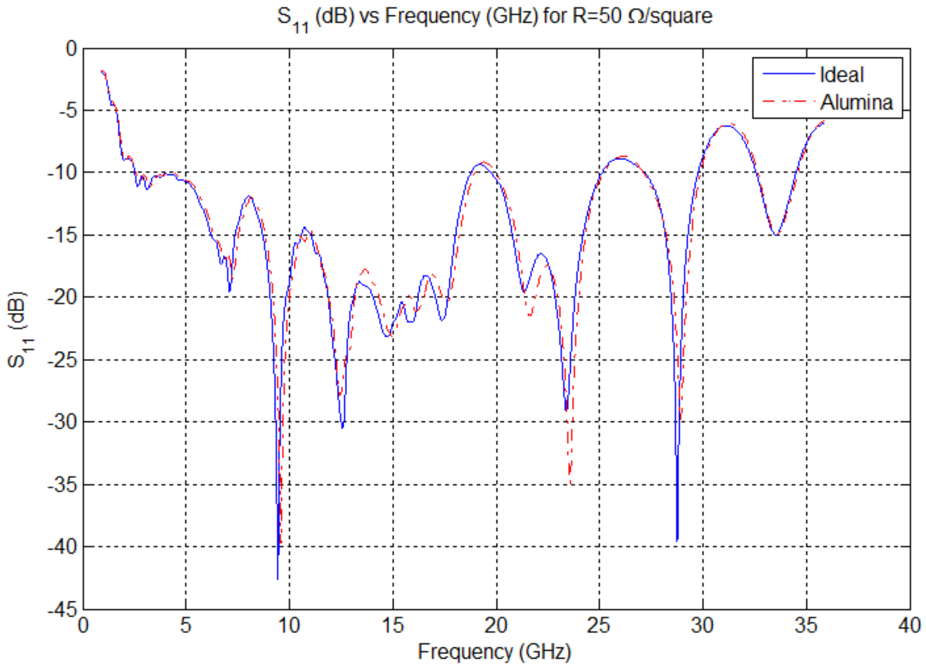

Figure 7.5. Comparison of the simulated return loss versus frequency for a 50 Ω/square antenna immersed in an ideal medium and Alumina.

The simulations have shown that, as predicted, Alumina provides the best return loss characteristics. This is due to the low mismatch between Alumina's ε_r of 9.6 and the best case scenario ε_r of 10.2. Since Alumina satisfied the low loss and low moisture absorption criteria as well, it is the most promising material for the mould to be machined from.

7.3 Discussion of Mould Shape and Slot Layout

In previous sections, we have already determined that the mould will be a hemi-spherical bowl shape with an inner radius of 7 cm and an outer radius of 8.5 cm. Aside from the basic dimensions of the mould, we also need to decide how many antenna slots it will have. The slots size, location and orientation are additional important factors. This section will describe the design decisions and process.

The initial design for the mould was drawn up by now-graduated Ph.D. student H. Kanj; Figure 7.6 shows his original layout (all mould drawings are done in SEMCAD-X). The inner and outer radii are the same as mentioned above, but the mould has a flat bottom instead of being hemi-spherical. There are eight slots for antennas, four each on opposite sides of the mould. The slots alternate in direction and are 0.635 x 15.8 x 12 mm, just large enough for an antenna to fit snuggly inside.

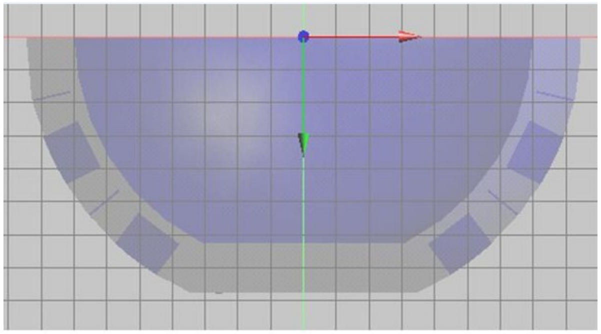

Figure 7.6. Initial mould design.

The first adaptation we make to the mould is to remove the flattened bottom. While the flat edge makes it easier to rest the mould on a table for experiments, we aim to have the breast phantom, and therefore the mould, as realistic as possible. Thus, the mould will be hemi-spherical in shape. A second adaptation is made necessary when looking at the drawings from a machining point of view. The slot width of only 0.635 mm is too small to be cut by the smallest sized drill bit available. Insisting on maintaining the 0.635 mm width could exponentially increase fabrication costs, if machining it would be possible at all. For this reason, we increase the slot width to 3 mm, thinking that we can fill the space surrounding the antennas with the matching gel.

It is at this step that a key idea develops. To further increase the ease of fabrication, we could make each slot 3 x 18 x 12 mm. Then inside the slot can be placed a ‘suitcase’, an enclosure which would hold the antenna tightly and itself fit tightly into the now larger slot. Figure 7.7 shows the updated mould, which now has a rounded bottom and larger slots. We also note that the centre of the slots are equally spaced around each side of the outer radius of mould. The slots still alternate in direction. Figure 7.8 shows the mould drawn with all the same dimensions as in Figure 7.7, but now the suitcases can be seen.

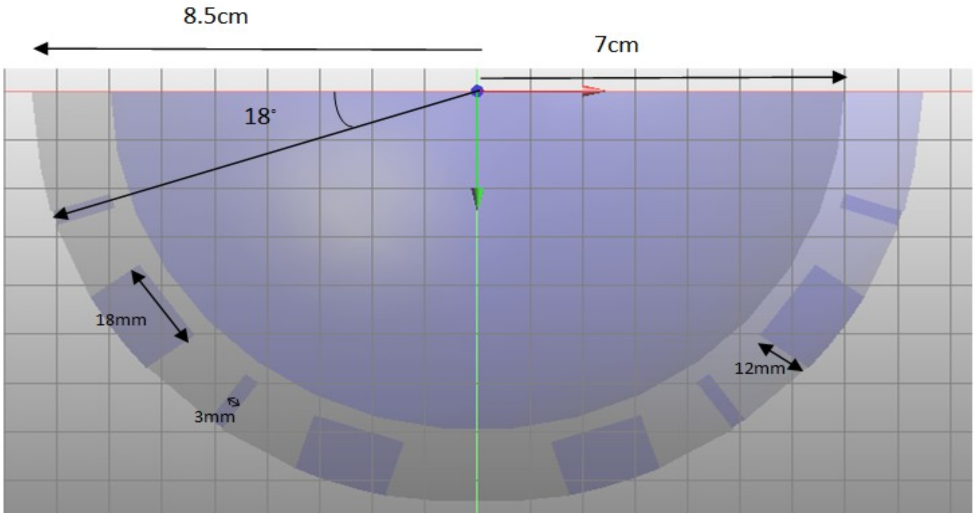

Figure 7.7. Updated drawing of the mould.

The idea of using a suitcase to surround the antenna within the slot solves the problem of having slots that are too small to manufacture, however it adds many more questions to this discussion. For instance, is this the best size the suitcase can be? Should it be made of the same material as the mould, or a different one? Also, will the S_{11} performance be negatively affected by the addition of more interfaces in front of the antenna? These questions will all be addressed through various simulations presented in the next section.

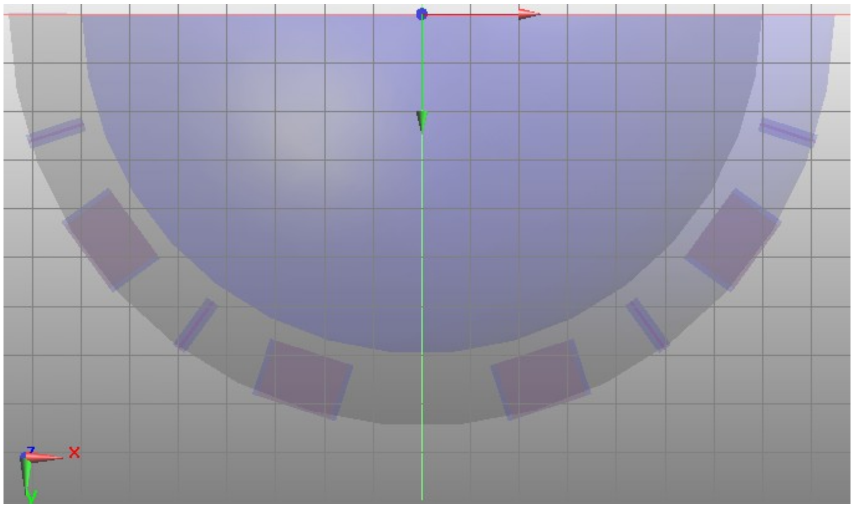

Figure 7.8. The mould with suitcases in the larger slots. The blue cut-away area from the slots is the size of the suitcases, while the red area is the size of the antenna within.

7.4 Investigation of the Mould with Suitcases

In this section, we assume that suitcases will be used to fill the slots in the mould, and we explore various designs for these suitcases. The main point of interest is that by using a material for the suitcase that has $\varepsilon_r \approx 10.2$ it may be possible to use a material for the mould that has a much lower relative permittivity and still obtain an overall return loss that is acceptable. Thus we begin this discussion with simulations in which an antenna is surrounded by a suitcase made from HiK ($\varepsilon_r = 10$), which is placed inside various mould materials. The HiK material is considered a good option for the suitcases since they would be relatively small and could easily be fabricated (unlike the mould itself).

Figure 7.9 shows the simulation results for three different antennas (surface resistivity of 50 Ω/square, 100 Ω/square and 200 Ω/square) placed in a suitcase made from HiK ($\varepsilon_r = 10$) in a mould made from Lexan ($\varepsilon_r = 4.4$). The performance is slightly better than in Figure 7.2 where the mould is made of Lexan and there are no suitcases. However, the return loss is above -10 dB for all three antennas up to 5 GHz, when the return loss goes below -10 dB for the 50 Ω/square antenna. Since we would like to have $S_{11} < -10$ dB from 3 GHz up, none of these scenarios involving a mould made of Lexan provide appropriate results. Once again, Lexan is discarded as being a potential mould material.

Figure 7.10 plots the simulated return loss for antennas in a HiK ($\varepsilon_r = 10$) suitcase within a Mycalex ($\varepsilon_r = 6.9$) mould. In this case, S_{11} is less than -10 dB from 3.5 GHz up to 19.2 GHz for the 50 Ω/square antenna (the one with best results). This is not far off from the performance we would hope to obtain, however using materials that provide better performance at lower frequencies would be beneficial.

The final scenario investigated is a mould that is made from Alumina, having $\varepsilon_r = 9.6$, with suitcases made from HiK ($\varepsilon_r = 10$). The simulated S_{11} parameter is shown in Figure 7.11. As for all scenarios, the performance at low frequencies is terrible for the 100 Ω/square and 200 Ω/square antennas. However, the simulation with the 50 Ω/square antenna is very promising. In this case, the return loss is less than -10 dB starting at 2.6 GHz extending way beyond our frequency range of interest. Figure 7.12 compares the simulated S_{11} for the 50 Ω/square antenna under three different conditions: an ideal mould ($\varepsilon_r = 10.2$), a mould of Alumina ($\varepsilon_r = 9.6$), and a mould of Alumina with HiK ($\varepsilon_r = 10$) suitcases. The return loss is virtually identical for all three cases, particularly in the 3-10 GHz frequency range.

Thus it is concluded that a mould made from Alumina that houses suitcases made from HiK would be a suitable solution. This combination would result in $S_{11} < -10$ dB from 3 to 10 GHz. It is also a scenario that could be fabricated easily. Simulations were also done with various suitcase sizes and mould sizes, neither of which has a significant effect on S_{11}.

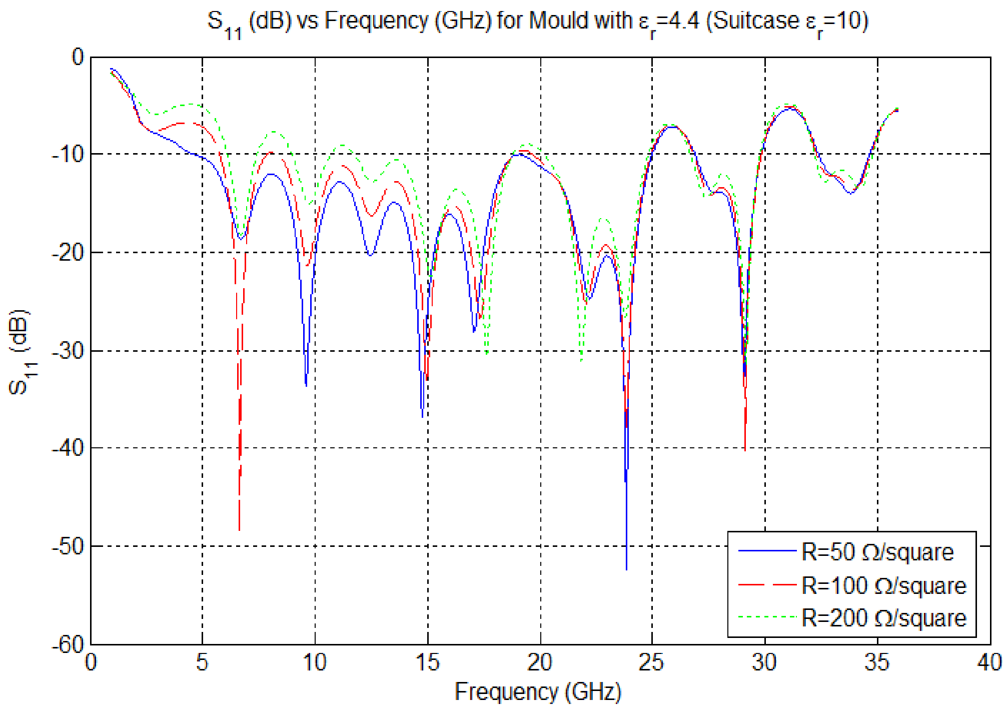

Figure 7.9. Plot of simulated S_{11} versus frequency for three antennas with a mould made from Lexan and suitcases from HiK.

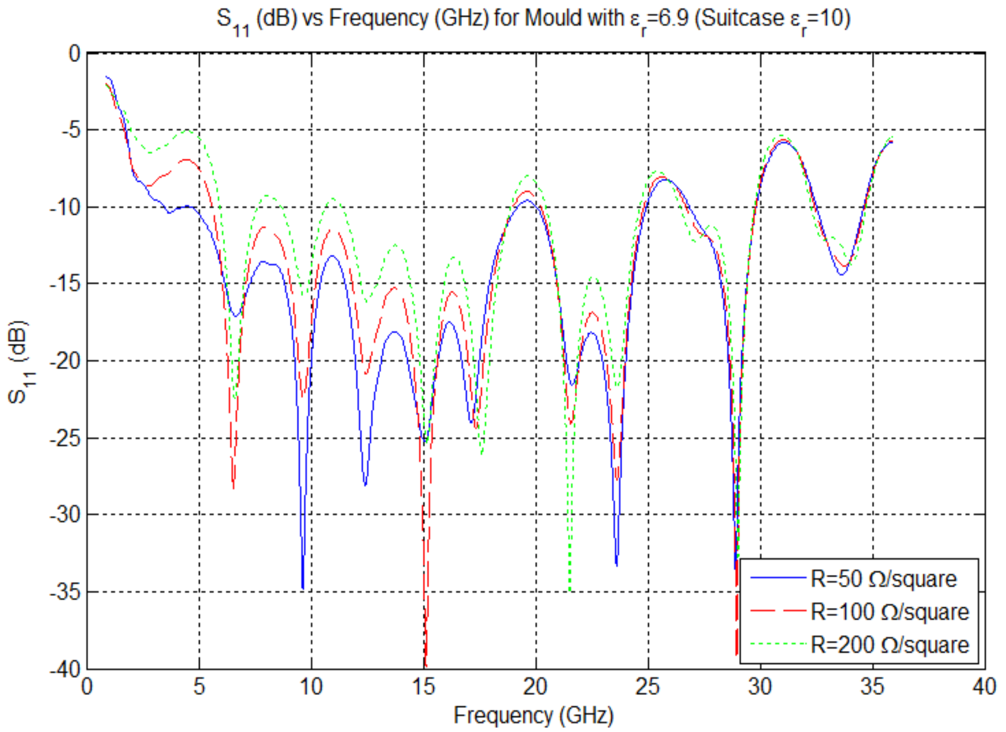

Figure 7.10. Plot of simulated S_{11} versus frequency for three antennas with a mould made from Mycalex and suitcases from HiK.

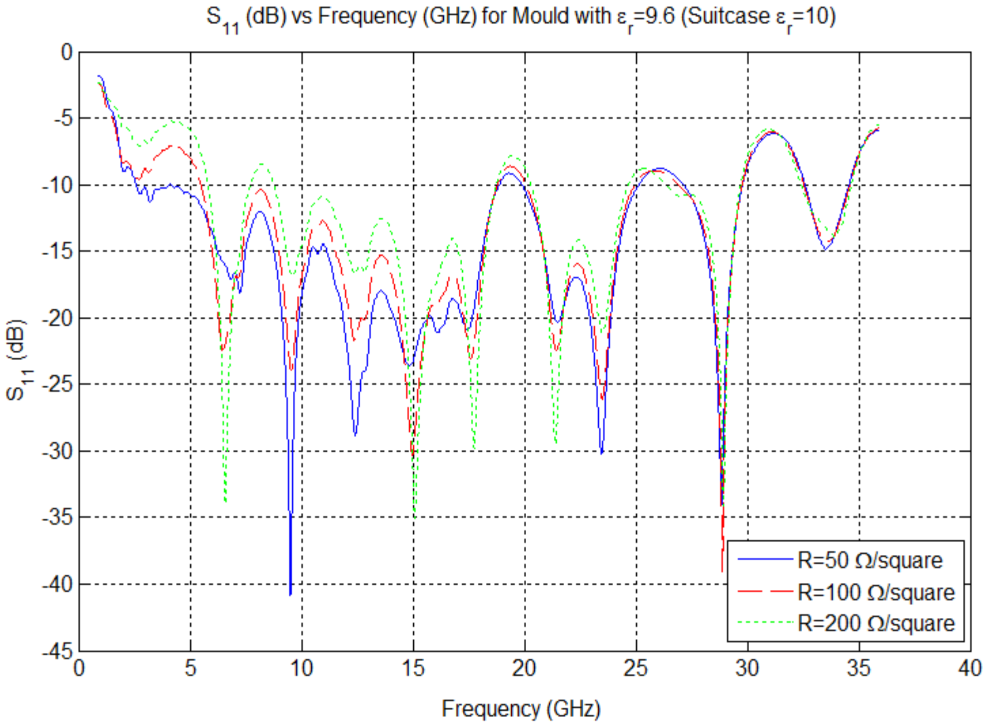

Figure 7.11. Plot of simulated S_{11} versus frequency for three antennas with a mould made from Alumina and suitcases from HiK.

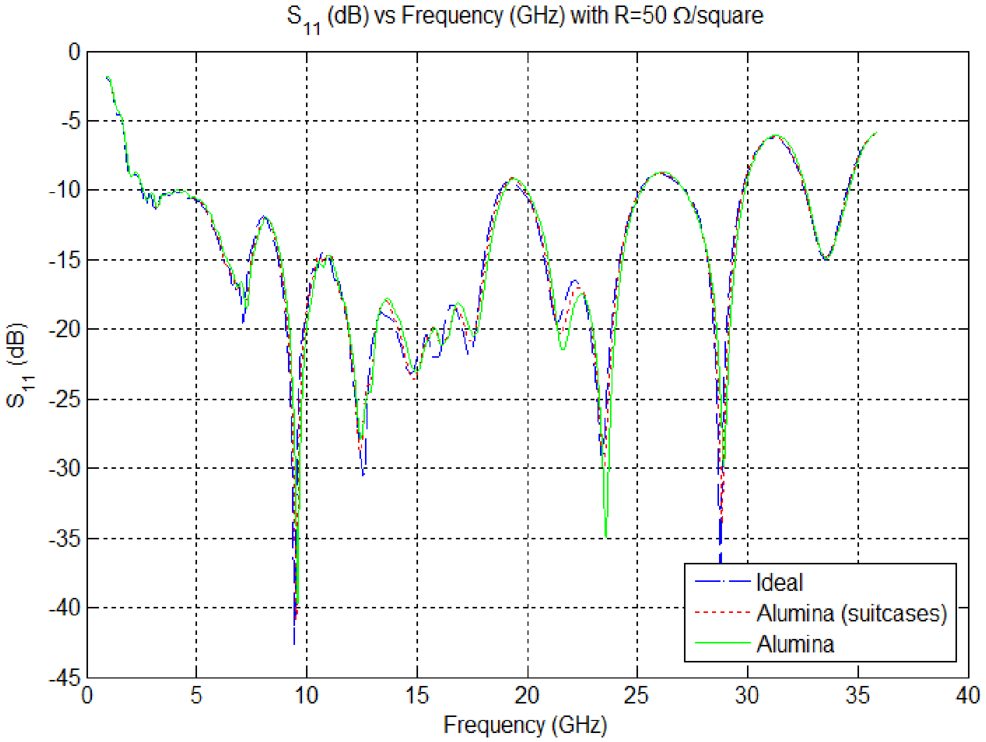

Figure 7.12. Plot of simulated S_{11} versus frequency for the 50 Ω/square antenna in a mould of ideal material (blue), a mould of Alumina (green) and a mould made from Alumina with HiK suitcases (red).

7.5 Summary of Chosen Design

This section presents the final design chosen for the mould and the suitcases. In this design, the mould has 16 slots along its outer surface; and each slot has dimension 3 x 18 x 13 mm. There are four slots on each side of the mould. Two sides of the mould have all slots in the same direction while the other two sides have slots that alternate in direction. The centres of the slots are equally spaced at 18 degree increments around the middle of the mould.

The purpose of having two sides with slots in the same direction and two sides with slots in alternating directions is to increase the ability of the mould to perform various test scenarios. For instance, we may look at signals transmitted through the mould and received by an antenna on the opposite side, or signals reflected back to reach antennas on the same side as the transmitter. We can also examine reflections between two antennas that are oriented in the same direction or oriented 90° apart. This allows for many testing possibilities to both further our understanding of microwave radar imaging and to determine which combination of transmitting and receiving antenna(s) leads to the best results.

A drawing of the final mould design with all relevant dimensions is given in Figure 7.13. Similarly, Figure 7.14 shows the same mould rotated 90° so that each of the sides can be seen clearly. The mould was ordered from Friatec and is made from Alumina. A photograph of it taken from above can be seen in Figure 7.15.

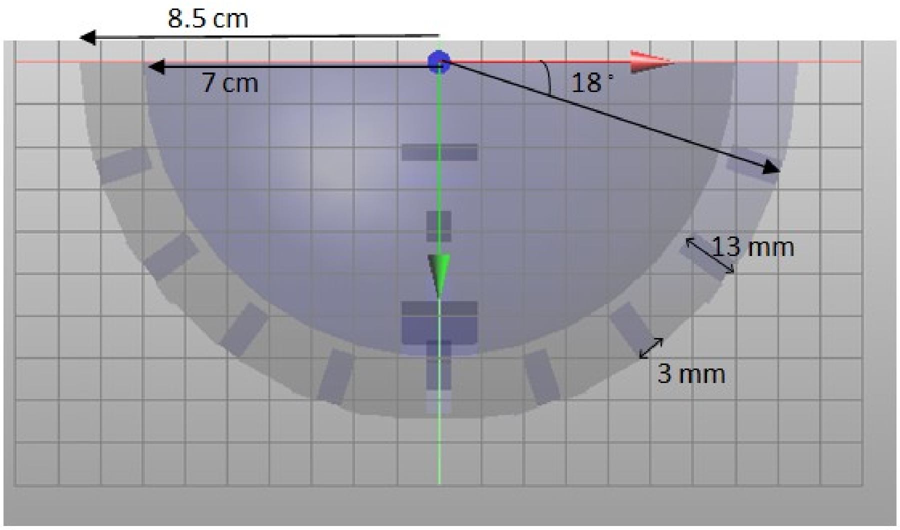

Figure 7.13. Drawing of the final mould design.

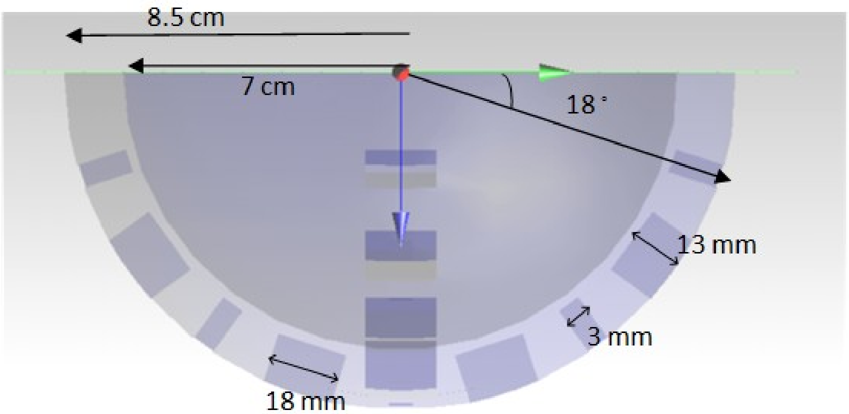

Figure 7.14. Drawing of the final mould design, rotated 90°.

Figure 7.15. Photograph of the mould.

Finally, HiK suitcases were ordered from Emerson and Cuming. Each suitcase, when put together, is 3 x 18 x 13 mm. In order to simplify fabrication, each suitcase is made in two pieces. The top piece is just rectangular with dimension 1.5 x 18 x 13 mm. The bottom piece is also 1.5 x 18 x 13 mm, with an antenna-sized grove cut out of it. A drawing of the bottom suitcase piece is shown in Figure 7.16. The antenna can be placed into the bottom piece, then the top piece is placed on top, and together they can be slid into the slot in the mould. Figure 7.17 shows photographs of both the top and bottom suitcase pieces.

As a side note, we also obtained plugs made from HiK. These are 3 x 18 x 13 mm bricks of material that can each fill a single slot. These will be used when the slots are not in use. For instance, if at a given time measurements are being performed using only two antennae instead of sixteen, then the remaining 14 empty slots will be filled with the plugs.

Once the suitcases and mould were delivered, some slight adjustments had to be done by hand to make all of the elements fit together. This is to be expected, since we desire the suitcase to fit tightly in the mould, and the components were made by different companies with different machining tolerances. In cases where the antenna did not fit into the suitcase, or the suitcase did not fit into the slot in the mould, the suitcase is easily filed (using a regular nail file) for a better fit. It is also important to note that since the suitcases do fit so tightly into the mould, tweezers or some form of pliers are needed to remove them.

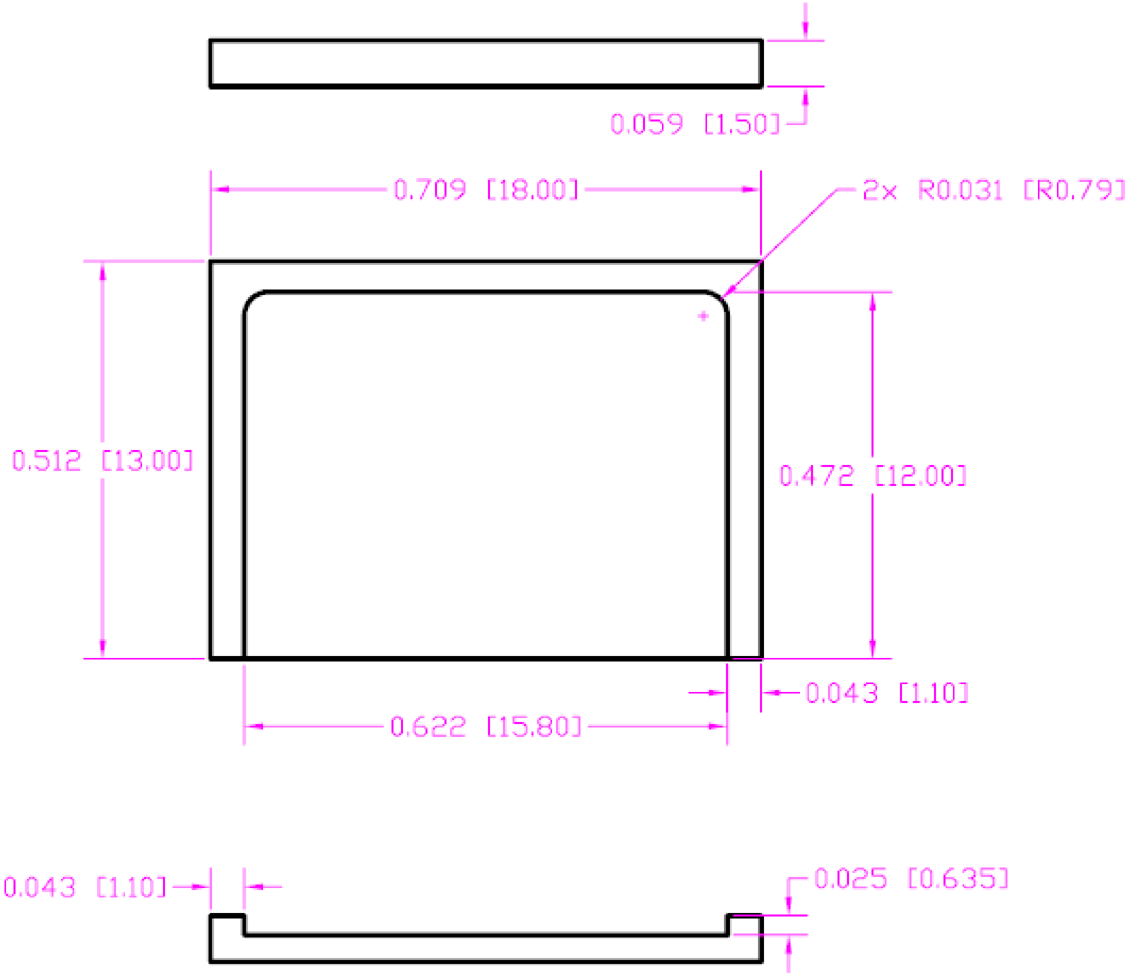

Figure 7.16. Schematic drawing of the bottom half of the suitcase (drawn by Emerson & Cuming): Back view (top drawing), top view (centre) and front view (bottom). The dimensions for each section are given in inches [centimetres].

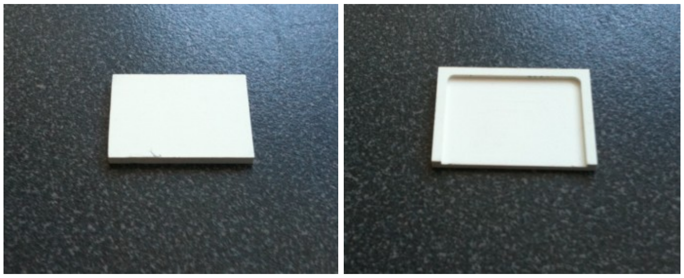

Figure 7.17. Photograph of the suitcase components. Top piece of suitcase (left) and bottom piece (right).

Chapter 8 Early Experimental Results

For these basic tests with the experimental system, we use a reduced number of components to decrease the complexity in testing. The scenario then becomes a simpler version of that depicted in Figure 3.1: the clock connects to the impulse generator and the picoscope, the impulse generator sends a signal to a transmitting antenna and one receiving antenna picks it up and sends it to the picoscope. Hence, only two out of the possible 16 antennas are used. We use only 50 Ω/square antennas.

A list of test cases is given in Table 8.1. The clock is set at 2 GHz for all of the measurements. The tumor used is 1.5 cm in size. All of the four test cases are performed in each of the following situations: antennas embedded in fat phantom, antennas embedded in a fat phantom with skin, antennas in the mould which holds a fat phantom, and antennas in the mould which holds a fat phantom with skin. When phantoms were used without the mould, in case 4 the antennas are next to each other and placed along the same plane; when the mould is used the antennas are next to each other (in slots that are at adjacent sides of the radome) but are oriented 90° apart. We also take two baseline measurements (measurements with the phantoms present but without any tumors) for each situation, one for antennas opposite each other (cases 1-3) and one for antennas beside each other (case 4).

Three measurements are recorded for each case and for the baselines. These are then averaged. To obtain the tumor response, the received signal and the corresponding baseline for that case are subtracted. Figures 8.1 through 8.4 show the tumor response for the four cases for the fat phantom, fat and skin phantom, fat phantom in mould, and fat and skin phantom in mould, respectively.

Table 8.1. List of experimental test cases.

Case number	Description
1	Tumor centred in fat phantom, antennas opposite each other
2	Tumor near receiver, antennas opposite each other
3	Tumor near transmitter, antennas opposite each other
4	Tumor near transmitter and receiver, antennas beside each other

It is clear from these measurements that using the mould results in significantly noisier tumor responses. This is most likely caused by the air gaps mentioned in Chapter 7, which should be corrected for in future measurements. Despite this, it is encouraging to note that a tumor response can clearly be detected even without the low-noise amplifiers. We also note that (in situations without the mould) the tumor response is much greater when the antennas are located beside each other instead of opposite each other. This is partly because when they are beside each other the tumor response does not need to travel as far through the fat (it is not attenuated as much). However, the response is misleading because the received signal exhibits a phase difference from the transmitted signal – if they were aligned then the subtraction would produce a smaller tumor response (on par with the other three cases).

Thus we have seen that for all tested cases, the magnitude of the tumor response is easily detectable, even though no low-noise amplifiers have been included. This is very encouraging, since the tumors we have tested with here are relatively large and had the tumor responses been close to the noise limit we would be forced to use more expensive and difficult to obtain low-noise equipment. It is also noted that the relative positioning of the transmitting and receiving antenna has a large effect on the obtained tumor response. This indicates that we could arrange the antennas in such a way as to optimize the tumor response, but more research will have to be done towards determining this optimal configuration.

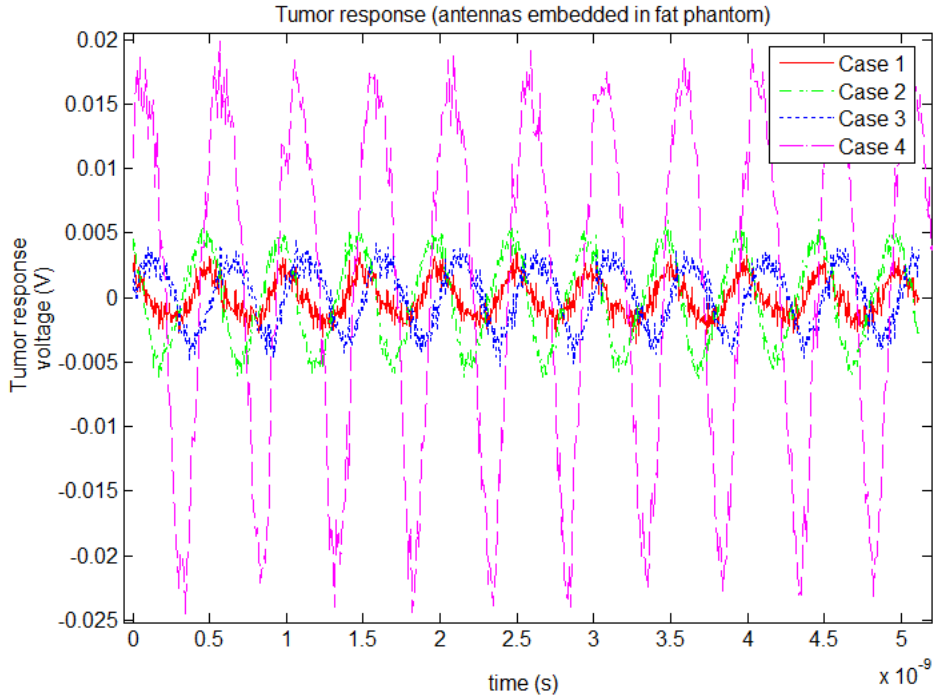

Figure 8.1. Plot of the tumor response when the antennas are embedded directly in the fat phantom.

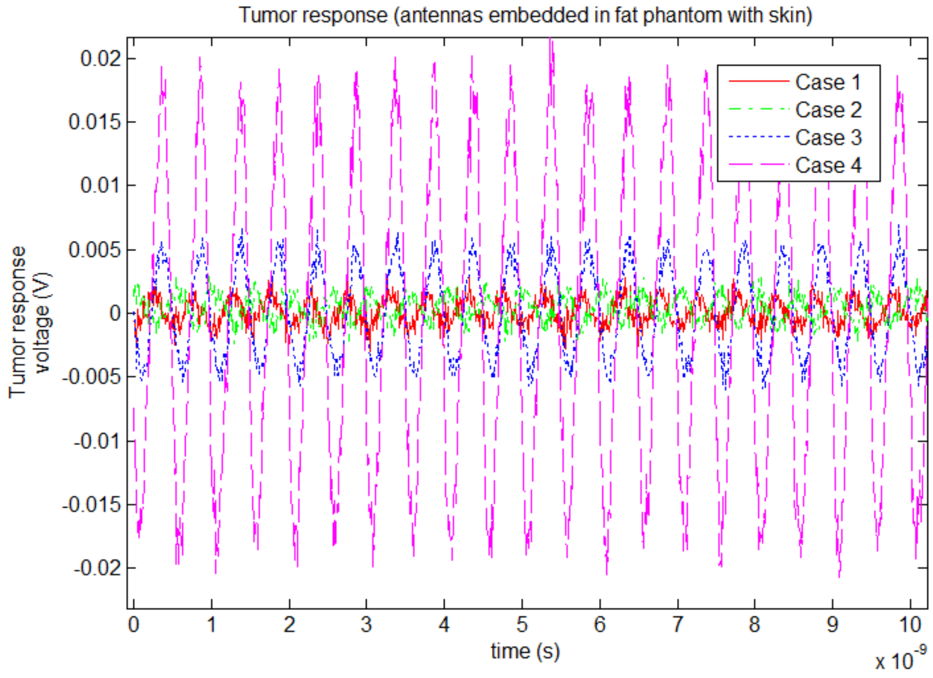

Figure 8.2. Plot of the tumor response when the antennas are embedded in a fat phantom with skin.

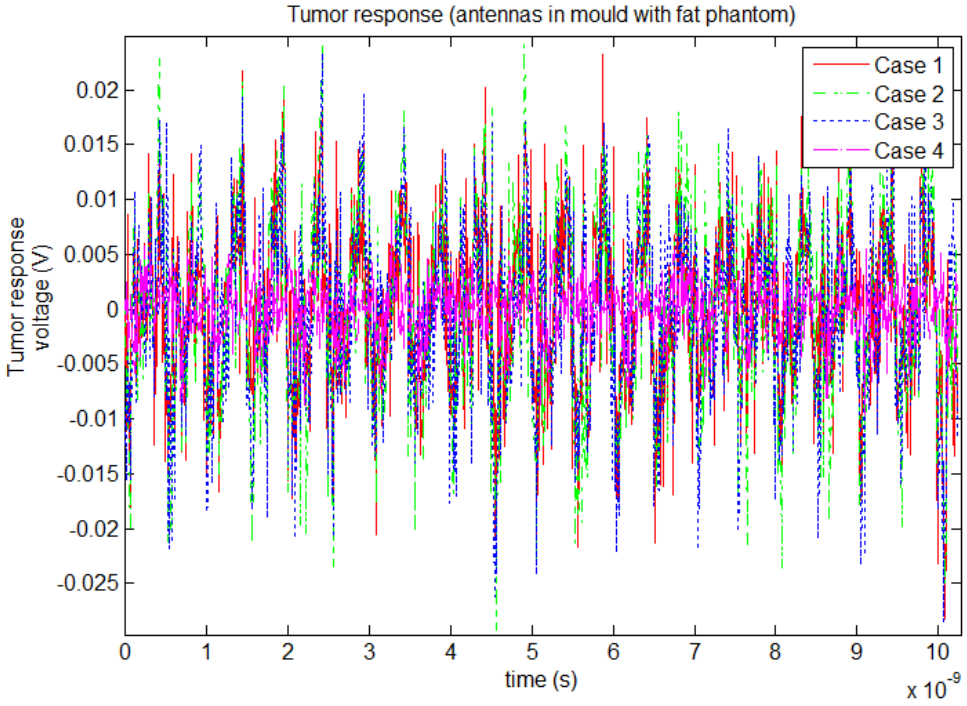

Figure 8.3. Plot of the tumor response when the antennas are in the mould, which holds a fat phantom.

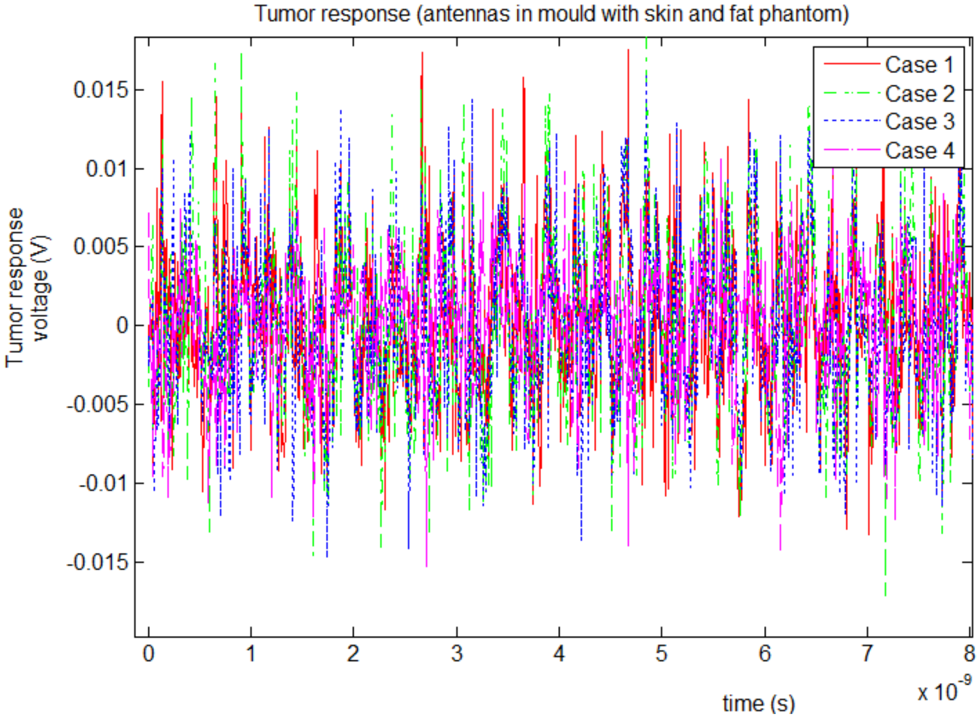

Figure 8.4. Plot of the tumor response when the antennas are in the mould, which holds a fat phantom with skin.

Chapter 9 Summary of Works Presented

Before concluding this thesis, this chapter will provide a brief summary of the work that has been presented here.

A system for microwave imaging of the breast in the time-domain has been introduced. Its standard components, as well as the specifically designed ones, are listed and their purposes described. In particular, the antenna and the mould are discussed in detail and corresponding simulations are shown.

We have given a procedure for making breast models for testing of microwave breast cancer detection. Both the numerical and experimental models are made as realistic as possible in terms of tissue properties and breast geometry. The numerical models are derived from MRI scans of the breast, and their tissue properties assigned according to tissue measurements from the literature. The experimental breast phantoms are mixed from easily obtainable chemicals (most significantly, oil and water) and their dielectric properties are adjusted also to match those from actual tissue measurements reported in the literature.

Finally, early experimental results using the proposed time-domain microwave imaging system are given. The early tests are done with two antennas (one transmitter and one receiver) and phantoms that have just one tumor and no glands. Results for breast phantoms with and without skin are shown for both cases of antennas in direct contact with the phantoms and antennas that are held in the mould.

Chapter 10 Conclusion and Future Work

This thesis has laid the foundation for experimental validation tests of microwave breast cancer detection. We have made progress with building more realistic breast phantoms. We have also presented a basic first set of tests imaging the phantoms with our system.

There are many areas in which this work will continue to be explored in the future:

- incorporation of the low-noise amplifiers and switches into the system;
- imaging of phantoms with different sized tumors and with phantoms that have more than one tumor;
- imaging of phantoms that have glandular tissue;
- more thorough investigation of imaging using two antennas that are opposite each other, beside each other, oriented along the same plane and oriented 90° apart;
- imaging using more than one receiving antenna (our system allows for up to 15);
- testing of various matching mediums.

Bibliography

[1] Canadian Cancer Society. (2009) What is breast cancer? [Online]. http://www.cancer.ca

[2] S.K. Moore, "Better Breast Cancer Detection," *IEEE Spectrum*, vol. 38, no. 5, pp. 50-54, 2001.

[3] American Cancer Society, "Cancer Facts & Figures 2008," American Cancer Society, Atlanta, 2008.

[4] E.C. Fear, P.M. Meaney, and M.A. Stuchly, "Microwaves for breast cancer detection?," *IEEE Potentials*, vol. 22, no. 1, pp. 12-18, 2003.

[5] A. Karellas and S. Vedantham, "Breast cancer imaging: a perspective for the next decade," *Med. Phys.*, vol. 35, no. 11, pp. 4878-4897, 2008.

[6] E.C. Fear, "Microwave Imaging of the Breast," *Technology in Cancer Research and Treatment*, vol. 4, no. 1, pp. 69-82, 2005.

[7] R.J. Halter et al., "The correlation of in vivo and ex vivo tissue dielectric properties to validate electromagnetic breast imaging: initial clinical experience," *Physiol. Meas.*, vol. 30, pp. 121-136, 2009.

[8] W.M.A. Ibrahim and H.M. Algabroun, "Family Tree of Breast Microwave Imaging Techniques," in *Biomed 2008, Proceedings 21*, 2008, pp. 258-261.

[9] E.C. Fear and M.A. Stuchly, "Microwave Detection of Breast Cancer," *IEEE Transactions on Microwave Theory and Techniques*, vol. 48, no. 11, pp. 1854-1863, 2000.

[10] Warren L. Stutzman and Gary A. Thiele, *Antenna Theory and Design*, 2nd ed.: Wiley, 1998, ch. 11.

[11] speag. (2008) SEMCAD X Reference Guide. [Online]. http://www.semcad.com/

[12] eHealthMD. (2010) Breast Anatomy. [Online]. http://www.ehealthmd.com/library/breastcancer/BRC_anatomy.html

[13] Sharon Mantik Lewis, Margaret McLean Heitkemper, and Shannon Ruff Dirksen, *Medical~Surgical Nursing in Canada: Assessment and Management of Clinical Problems*, 1st ed., S. Goldsworthy and Maureen Barry, Eds. Toronto, Canada:

Elsevier Canada, 2006.

[14] Infrared Medical Solutions. (2010) Understanding Breast Physiology. [Online]. http://www.infraredmedicalsolutions.com/patients/about_breast_physiology

[15] M. Lazebnik et al., "A large-scale study of the ultrawideband microwave dielectric properties of normal breast tissue obtained from reduction surgeries," *Phys. Med. Biol.*, vol. 52, pp. 2637-2656, 2007.

[16] Mariya Lazebnik, Michal Okoniewski, John H. Booske, and Susan C. Hagness, "Highly Accurate Debye Models for Normal and Malignant Breast Tissue Dielectric Properties at Microwave Frequencies," *IEEE Microwave and Wireless Components Letters*, vol. 17, no. 12, pp. 822-824, December 2007.

[17] M. Lazebnik et al., "A large-scale study of the ultrawideband microwave dielectric properties of normal, benign and malignant breast tissue obtained from cancer surgeries," *Phys. Med. Biol.*, vol. 52, pp. 6093-6115, 2007.

[18] M. Lazebnik, E. Madsen, G. Frank, and S. Hagness, "Tissue-mimicking phantom materials for narrowband and ultrawideband microwave applications," *Phys. Med. Biol.*, vol. 50, pp. 4245-4258, 2005.

[19] S. Gabriel, R.W. Lau, and C. Gabriel, "The dielectric properties of biological tissues: III. Parametric models for the dielectric spectrum of tissues," *Phys. Med. Biol.*, vol. 41, pp. 2271-2293, 1996.

[20] J. Croteau, J. Sill, T. Williams, and E. Fear, "Phantoms for testing radar-based microwave breast imaging," in *13th International Symposium on Antenna Technology and Applied Electromagnetics and the Canadian Radio Science Meeting, 2009. ANTEM/URSI 2009*, 2009, pp. 1-4.

[21] I.J. Craddock et al., "Development of a Hemi-spherical Wideband Antenna Array for Breast Cancer Imaging," in *First European Conference on Antennas and Propagation, 2006. EuCAP 2006*, 2006, pp. 1-5.

[22] I.J. Craddock, M. Klemm, J. Leendertz, A.W. Preece, and R. Benjamin, "An Improved Hemi-spherical Antenna Array Design for Breast Imaging," in *The Second European Conference on Antennas and Propagation, 2007. EuCAP 2007*, 2007, pp. 1-5.

[23] M. Klemm, I.J. Craddock, J. Leendertz, A.W. Preece, and R. Benjamin, "Breast Cancer Detection using Symmetrical Antenna Array," in *The Second European Conference on Antennas and Propagation, 2007. EuCAP 2007*, 2007, pp. 1-5.

[24] I.J. Craddock, M. Klemm, J. Leendertz, A.W. Preece, and R. Benjamin, "Development and application of a UWB radar system for breast imaging," in *Antennas and Propagation Conference, 2008. LAPC 2008*, 2008, pp. 24-27.

[25] M. Klemm, I.J. Craddock, J.A. Leendertz, A. Preece, and R. Benjamin, "Radar-Based Breast Cancer Detection Using a Hemispherical Antenna Array—Experimental Results," *IEEE Transactions on Antennas and Propagation*, vol. 57, no. 6, pp. 1692-1704, 2009.

[26] M. Klemm et al., "Clinical Trials of a UWB Imaging Radar for Breast Cancer," in *The Fourth European Conference on Antennas and Propagation, 2010. EuCAP 2010.*, Barcelona, 2010.

[27] S.M. Salvador and G. Vecchi, "Experimental Tests of Microwave Breast Cancer Detection on Phantoms," *IEEE Transactions on Antennas and Propagation*, vol. 57, no. 6, pp. 1705-1712, 2009.

[28] P.M. Meaney, M.W. Fanning, L. Dun, S.P. Poplack, and K.D. Paulsen, "A clinical prototype for active microwave imaging of the breast," *IEEE Transactions on Microwave Theory and Techniques*, vol. 48, no. 11, pp. 1841-1853, 2000.

[29] P.M. Meaney et al., "Clinical microwave breast imaging – 2D results and the evolution to 3D," in *International Conference on Electromagnetics in Advanced Applications, 2009. ICEAA 2009*, 2009, pp. 881-884.

[30] T.L. Pope Jr, M.E. Read, T. Medsker, A.J. Buschi, and A.N. Brenbridge, "Breast skin thickness: normal range and causes of thickening shown on film-screen mammography," *Journal of the Canadian Association of Radiologists*, vol. 35, no. 4, pp. 365-368, 1984.

[31] G. Zhu, B. Oreshkin, E. Porter, M. Coates, and M. Popović, "Dispersive Breast Models for Efficient FDTD Simulation," in *The Third European Conference on Antennas and Propagation, 2009. EuCAP 2009*, 2009.

[32] E.C. Fear and M.A. Stuchly, "Confocal microwave imaging for breast tumor detection: comparison of immersion liquids," *IEEE Antennas and Propagation Society International Symposium*, vol. 1, pp. 250-253, 2001.

[33] Emily Porter, Jules Fakhoury, Razvan Oprisor, Mark Coates, and Milica Popovic, "Improved Tissue Phantoms for Experimental Validation of Microwave Breast Cancer Detection," in *The Fourth European Conference on Antennas and Propagation (EuCAP 2010)*, Barcelona, 2010.

[34] E. Zastrow, S. Davis, M. Lazebnik, F. Kelcz, and S. Hagness, "Development of Anatomically Realistic Numerical Breast Phantoms With Accurate Dielectric Properties for Modeling Microwave Interactions With the Human Breast," *IEEE Transactions on Biomedical Engineering*, vol. 55, no. 12, pp. 2792-2800, 2008.

[35] S. Gabriel, R.W. Lau, and C. Gabriel, "The dielectric properties of biological tissues: II. Measurements in the frequency range 10 Hz to 20 GHz," *Phys. Med. Biol.*, vol. 41, pp. 2251-2269, 1996.

[36] A.C. Guyton and J.E. Hall, *Textbook of Medical Physiology*, 11th ed.: Saunders, 2005.

[37] C. Shannon, M. Okoniewski, and E. Fear, "A dielectric filled ultra-wideband antenna for breast cancer detection," *IEEE Antennas and Propagation Society International Symposium*, vol. 1, pp. 218-221, 2003.

[38] H. Kanj and M. Popović, "Microwave-range broadband “dark eyes” antenna: detailed analysis and design," *IEEE Antennas and Wireless Propagation Letters*, vol. 4, pp. 262-265, 2005.

[39] H. Kanj, "A Novel Ultra-Compact Broadband Antenna for Microwave Breast Tumor Detection (Chapter 7)," *PhD thesis, Department of Electrical & Computer Engineering, McGill University, Montreal*, 2007.

[40] H. Kanj and M. Popovic, "A Novel Ultra-Compact Broadband Antenna for Microwave Breast Tumor Detection," *Progress in Electromagnetics Research (PIER)*, vol. 86, pp. 169-198, 2008.

[41] Federal Communications Commission (FCC). (2010) [Online]. http://www.fcc.gov